Universidad Carlos III de Madrid

Escuela Politécnica superior

Departamento de Ciencia e Ingeniería de Materiales

En colaboración con:

imdea materiales

Trabajo Fin de Grado:

Microstructural design in TiAl with high cooling rates

Autor: Raúl García González

Titulación: Grado en Ingeniería Aeroespacial

Tutor Universidad: Dr. José Manuel Torralba Castelló

Tutores IMDEA Materiales: Dr. Ilchat Sabirov y Dra. Ma Teresa Pérez Prado

Leganés, junio de 2015

Acknowledgements

The best kind of effort is that one whose consequences are above your expectations. The dedication of many persons has made this end of degree experience to be of that kind.

First, I would like to express my gratitude to Dr. Ilchat Sabirov, whose initial idea of microstructural design in TiAl, together with his continuous guidance to achieve the desired processing of the material, enabled the development of this study. This study would not have been possible without the support of María Teresa Pérez Prado. She was always there whenever you didn't know the way to continue. The labour of Alberto Palomares is highlighted by its own weight. He has transmitted, with a lot of dedication and enthusiasm a huge amount of information regarding material science research and TiAl particular characteristics.

I consider this is the best experience I could have had with any end of degree project. And the reasons for it have been the persons that have made it possible: THANK YOU.

Abstract

Gamma titanium aluminides are intermetallic alloys with great potential for aerospace applications in advanced aerospace engine and high-temperature airframe components and, in particular, in low pressure turbines (LPT), because they can provide increased thrust-to-weight ratios and improved efficiency under aggressive environments at temperatures up to 750 °C. Thus, γ-TiAl alloys are projected to replace the heavier Ni-base superalloys currently used for LPT blades manufacturing. These alloys offer low density, high specific strength, creep and corrosion resistance at high temperatures. Figure 1 compares their mechanical behavior with that of other high temperature alloys at a wide range of temperatures. However, the wide commercialization of gamma titanium aluminides is prevented by their low ductility as well as by the lack of quantitative models relating the microstructure and the mechanical behavior. Moreover, their full potential has not been exploited because a thorough knowledge on the possibilities for microstructural development upon cooling from the liquid phase or from high temperature phase domains is still lacking.

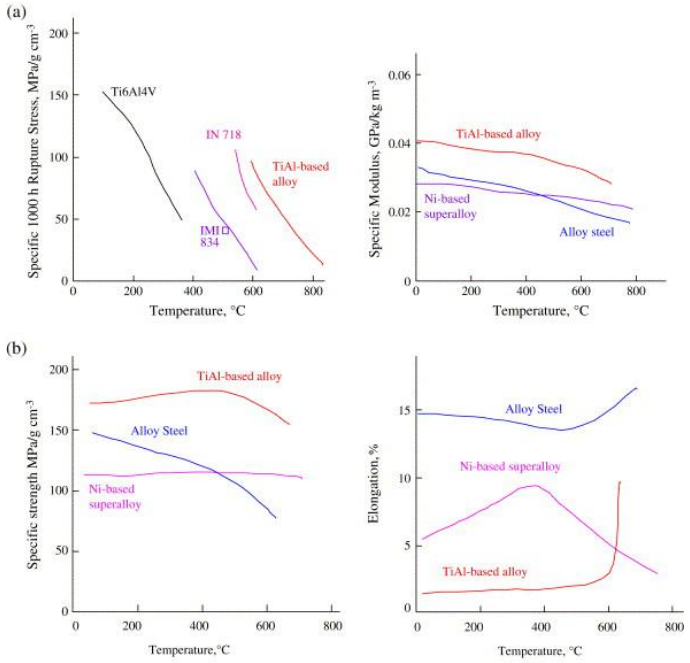

Figure 1. Comparison of the mechanical properties of TiAl alloys with those of other materials.

The aim of this project is to contribute to fill this knowledge gap by taking advantage of *Gleeble* technology and, in particular, of the possibility to use extremely high and well measured cooling rates to generate novel microstructures in a Ti-45Al-2Nb-2Mn(at.%)+0.8(vol.%)TiB_2 (Ti4522XD) alloy. The developed microstructures are thoroughly characterized by optical,

scanning and transmission electron microscopy and a link with their mechanical behavior, evaluated by hardness measurements, is established.

Index

1. Introduction

1.1 Intermetallics

The term “intermetallics” has been used to designate the intermetallic phases and compounds which result from the spatially-ordered combination of various metals, and which form a large class of materials [1]. There are mainly three types of superlattice structures based on the f.c.c. lattice: $L1_2$ (with a variant of $L1_2'$ in which a small interstitial atom of C or N is inserted at the cube center), $L1_0$, and $L1_2$-derivative long-period structures such as DO_{22} or DO_{23}. The b.c.c.-type structures are $B2$ and DO_3 or $L2_1$. The DO_{19} structure is one of the most typical superlattices based on h.c.p. symmetry. Table 1 lists the crystal structure, lattice parameter and density of selected intermetallic compounds [2]. A comprehensive review on the physical metallurgy and processing of intermetallics can be found in [3].

Alloy	**Structure (Bravais lattice)**	**Lattice Parameters**		**Density (g/cm^3)**
		$\mathbf{a\ (nm)}$	$\mathbf{c\ (nm)}$	
$\mathbf{Ni_3Al}$	$L1_2$ (simple cubic)	0.357	-	7.40
NiAl	$B2$ (simple cubic)	0.288	-	5.96
$\mathbf{Ni_2AlTi}$	DO_3	0.585	-	6.38
$\mathbf{Ti_3Al}$	DO_{19}	0.577	0.464	4.23
TiAl	$L1_0$	0.398	0.405	3.89
$\mathbf{Al_3Ti}$	DO_{22}	0.395	0.860	3.36
FeAl	$B2$ (simple cubic)	-	-	5.4-6.7 [4]
$\mathbf{Fe_3Al}$	DO_3	-	-	5.4-6.7 [4]
$\mathbf{MoSi_2}$	$C11$	-	-	6.3

Table 1. Crystal structure, lattice parameters and density of selected intermetallic compounds.

Intermetallics have high melting temperatures (usually higher than 1000ºC), due partly to the strong bonding between unlike atoms, which is, in general, a mixture between metallic, ionic and covalent to different extents. The presence of these strong bonds also results in high creep resistance. Another factor that contributes to the superior strength of intermetallics at elevated temperature is the high degree of long-range order [5].

The effect of order is, first, to slow diffusivity. The reason for this is that the number of atoms per unit cell is large in a material with long-range order. Therefore in alloys in which dislocation climb is rate-controlling, a decrease in the diffusion rate would result in a drop in the creep rate and therefore in an increase of the creep resistance. Secondly, the presence of a high degree of

long-range order may retard the viscous motion of dislocations. This is due to the fact that, when a dislocation moves, the long-range order is damaged and this leads to an opposing dragging force. Thus, the presence of order results in a decrease of the creep rate in the intermetallic alloys in which the mechanism of viscous glide of dislocations is rate-controlling. A practical example supporting this explanation is the use of single-crystal blades in turbo engines in order to minimize efficiency losses and wear caused by creep.

One major disadvantage of these materials, that is limiting their industrial application, is brittleness [6]. This is attributed to several factors. First, the strong atomic bonds as well as the long-range order give rise to high Peierls stresses. Transgranular cleavage will occur in a brittle manner if the latter are larger than the stress for nucleation of a crack. Second, grain boundaries are intrinsically weak. The low boundary cohesion results in part from the directionality of the distribution of the electronic charge in ordered alloys [3]. The strong atomic bonding between the two main alloy constituents is related to the p-d orbital hibridization, which leads to a strong directionality in the charge distribution. In grain boundaries the directionality is reduced and thus the bonding becomes much weaker. Other factors that may contribute to the brittleness in intermetallics are the limited number of operative slip systems, segregation of impurities at grain boundaries, a high-work hardening rate, planar slip, and the presence of constitutional defects. The latter may be, for example, atoms occupying sites of a sublattice other than their own sublattice (antisites) or vacancies of deficient atomic species (constitutional vacancies). The planar faults, dislocation dissociations, and dislocation core structures typical of intermetallics were summarized by Yamaguchi and Umakoshi [7]. Other so-called extrinsic factors that cause brittleness are the presence of segregants, interstitials, moisture in the environment, poor surface finish, and hydrogen [8]. It appears that those intermetallics with more potential as high-temperature structural materials, i.e., those which are less brittle, are compounds with high crystal symmetry and small unit cells. Thus, nickel aluminides, titanium aluminides, and iron aluminides have been the subject of the most activities in research and development over the last two decades. These investigations were stimulated by both the possibility of industrial application and scientific interest [1-10].

Creep resistance is a critical property in materials used for high temperature structural applications. Some intermetallics may have the potential to replace nickel superalloys in parts such as the rotating blades of gas turbines or jet engines [11] due to their higher melting temperatures, high oxidation and corrosion resistance, high creep resistance, and, in some cases, lower density. The creep behavior of intermetallics is more complicated than that of pure metals and disordered solid solution alloys due to their complex structures together with the varieties of chemical composition [12-13]. The rate-controlling

mechanisms are still not fully understood despite the significant efforts over the last couple of decades [1,7, 14-22].

1.2 Gamma TiAl alloys

Titanium aluminide alloys have potential for replacing heavier materials in high temperature structural applications such as automotive and aerospace engine components. This is due, first, to their low density (lower than that of most other intermetallics), high melting temperature, good elevated temperature strength and high modulus, high oxidation resistance and favorable creep properties [23,24]. Second, they can be processed through conventional manufacturing methods such as casting, forging and machining [10]. In fact, TiAl turbocharger turbine wheels have recently been used in automobiles [10].

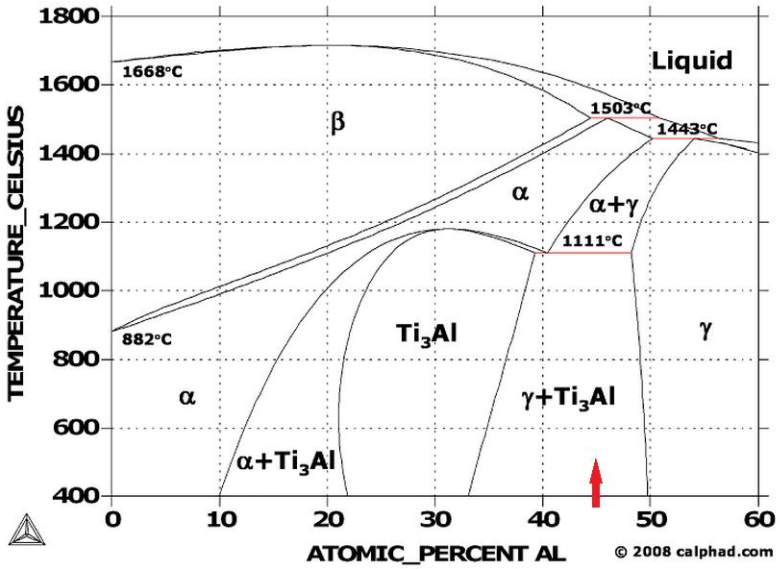

Figure 2. TiAl phase diagram.

Figure 2. the TiAl phase diagram, illustrates the following phases: γ-TiAl (ordered f.c.c. tetragonal, $L1_0$), α_2-Ti_3Al (ordered h.c.p., DO_{19}), α-Ti (h.c.p., high-temperature disordered), and β-Ti (b.c.c., disordered). α_2 alloys contain from 22at.% to approximately 35at.% Al. Gamma (γ) or near-γ TiAl alloys have compositions with 49-66 at.% Al, depending on temperature. Two-phase (γ-TiAl+α2- Ti3Al) alloys contain intermediate concentrations of aluminum, between 35at.% and 49at.% Al. The crystal lattices for γ-TiAl and α_2-Ti_3Al phases, the most relevant in this study, can be observed in figure 3.

Several microstructures can be developed in TiAl alloys, depending on the thermo-mechanical treatment. According to the relative fraction of equiaxed grains and lamellar colonies (grains composed of stacked planes of different phases), four microstructures can be distinguished: near-gamma (NG), with equiaxed γ-TiAl grains, duplex (DP), with a similar proportion of γ-TiAl grains and lamellar (α_2+γ) colonies, nearly lamellar (NL), with a greater amount of

lamellar colonies and fully lamellar (FL), where the whole volume is composed of lamellar colonies [25].

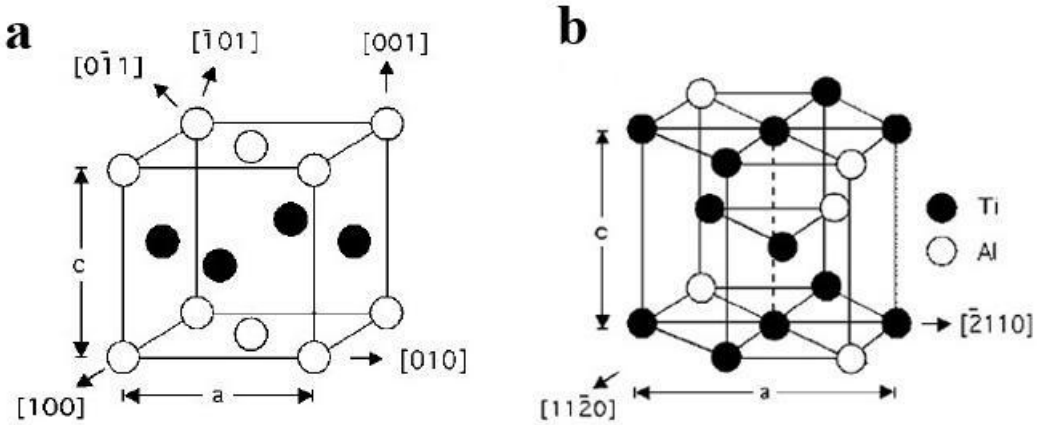

Figure 3. Cristal structures of a) γ-TiAl ($L1_0$) and b) α_2-Ti_3Al (DO_{19}) [26].

The morphology of the two phases depends on the thermomechanical processing [10]. Alloys, for example, with nearly stoichiometric or Ti-rich compositions that are cast or cooled from the β phase, going through the α single phase region and α→α+γ and α+γ → α_2 + γ reactions, have fully lamellar (FL) microstructures, as illustrated in Figure 4.

Figure 4. An example of a fully lamellar microstructure.

A FL microstructure consists of “lamellar grains”, of size g_l, that are equiaxed grains composed of thin alternating lamellae of γ and α_2. The average thickness of the lamellae, termed the lamellar interface spacing, is denoted by λ_l. The γ and α_2 lamellae are stacked such that {111} planes of the γ lamellae are parallel to (0001) planes of the α_2 lamellae and the closely packed directions on the former are parallel to those of the latter. The lamellar structure is destroyed if a FL microstructure is annealed or hot worked at temperatures higher than 1150ºC within the (α+γ) phase fields. A bimodal microstructure develops, consisting on lamellar grains alternating with γ grains (or grains exclusively of γ-phase). Depending of the amount of γ-grains, the microstructure is termed “nearly lamellar” (NL) when the fraction of γ-grains is small, or duplex

(DP) when the fractions of lamellar and γ-grains are comparable. Detailed studies of the microstructures of TiAl alloys are described in [27-28].

The cooling rates that have been used to generate the above microstructures in TiAl do not exceed 200ºC/s [29]. Greater cooling rates require no manipulation time and therefore cannot be reached manually. The current availability of physical simulation systems, like *Gleeble-3800*, enable the application of a water jet on the sample within milliseconds, thus opening a wide range of processing possibilities that remained unexplored until now.

1.3 Creep behavior of gamma titanium alumindes

Many investigations have attempted to understand the creep mechanisms in titanium aluminides over the last two decades. Several excellent reviews in this area include [10,30,31]. The creep behavior of titanium aluminides depends strongly on alloy composition and microstructure. Overall, two phase γ-TiAl alloys have more potential for high temperature applications than α-Ti_3Al alloys due to their higher oxidation resistance and elastic modulus [24]. Simultaneously, two-phase γ-TiAl alloys have comparatively lower creep strength at high temperature than α-Ti_3Al alloys and therefore significant efforts have been devoted in recent years to improve the creep behavior of γ-TiAl. It is now well established that, among the currently known microstructures, fully lamellar (FL) [32-34] two phase alloys offer the optimum creep resistance, the lowest minimum creep rate, and the best primary creep behavior (i.e., longer times to attain a specified strain). Lamellar microstructures have also superior fracture toughness and fatigue resistance than duplex (DP) structures, although the latter have, in general, better ductility [10]. Since the creep behavior of FL TiAl alloy is influenced by many different microstructural features, it is difficult to formulate a model that incorporates all of the relevant variables.

The use of *Gleeble* technology and, in particular, the combination of extremely high cooling rates with thermomechanical processing, could allow to develop novel microstructures with even better mechanical behavior than those available at the moment. In summary, a wide array of possibilities exist for the design of new microstructures in gamma TiAl alloys and, thus, the relationship between the microstructure and the mechanical behavior of these materials remains unexplored to a large extent. Significant efforts must be devoted in this direction in order to facilitate the commercialization of these materials.

2. Objectives

The aim of this project is to contribute to the understanding of microstructural design in gamma TiAl alloys by taking advantage of *Gleeble* technology and, in particular, of the possibility to use extremely high and well controlled cooling rates to generate novel microstructures in a Ti-45Al-2Nb-2Mn(at.%)+0.8(vol.%)TiB_2 (Ti4522XD) alloy.

More precisely, in this project, several microstructures have been generated in the mentioned TiAl alloy via quenching from the α phase region using a very wide range of cooling rates, including extreme values, not reachable manually. Additionally, samples have been processed by dynamic plastic deformation in the α phase region followed by quenching at extreme rates. Furthermore, the effect of annealing time before quenching has also been explored.

A thorough characterization of the developed microstructures has been carried out using optical, scanning and transmission electron microscopy. In particular, microstructural aspects such as the fraction of different phases, the grain geometry, the texture, the presence of macrodefects (cracks) have been systematically evaluated. Moreover, the mechanical behavior of the developed microstructures has been analyzed by the microhardness Vickers indentation test.

With all the above data, a link between the microstructures and their mechanical behavior is established and recommendations for the design of advanced TiAl alloys are derived.

3. Experimental procedure

3.1 Raw material

The studied alloy composition is: $\mathrm{Ti\text{-}45Al\text{-}2Nb\text{-}2Mn\text{-}0.8vol\%TiB_2}$.

The specimens to be processed and analyzed are straight circular bars with a diameter of 10 mm and a length varying between 8 and 11 cm. See figure 5.

Figure 5. Specimen geometry.

The specimens were machined by electrical wire cutting out of cast ingots produced by Access Technology. A portion of the ingot from which all bars were extracted can be seen in figure 6.

Figure 6. Cast material from which specimens were extracted.

3.2 Processing

A *Gleeble-3800* physical simulation system has been used to precisely control the processing of each of the samples. The overall layout of this machine can be seen in figure 7, where a) is the control unit and b) is the test bench. The temperature of the specimen is controlled by comparing its actual

temperature with the programmed temperature. The input electrical power to the sample is varied continuously in order to reduce this temperature difference. The power input to the sample is related to its heat rate (and thus its temperature) through the Joule effect. The actual specimen temperature is measured with a thermocouple. According to the temperature range specifications, see table 2, the used thermocouple combination was the Type R: Pt-13%Rh(+) and Pt(-).

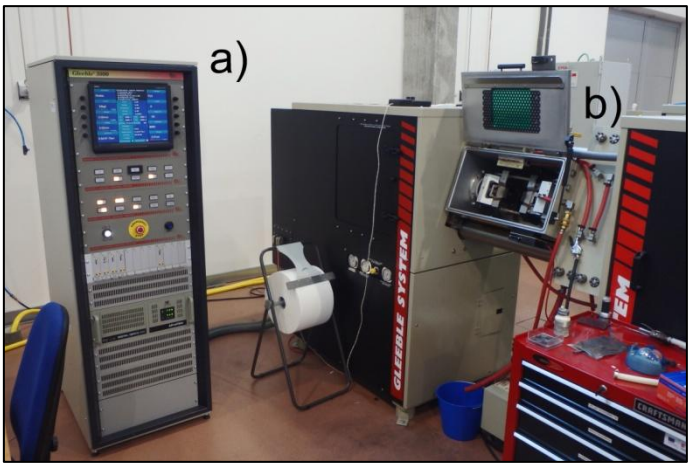

Figure 7. *Gleeble-3800* physical simulation machine.

TC type	Description	Operating Range
Type K	Ni-Cr(+) vs. Ni-Al(-)	0-1250 ºC
Type S	Pt-10%Rh(+) vs. Pt(-)	0-1450 ºC
Type R	Pt-13%Rh(+) vs. Pt(-)	0-1450 ºC
Type B	Pt-30%Rh(+) vs. Pt-6%Rh(-)	0-1700 ºC
Type E	Cu-Ni(+) vs. Ni-Cu(-)	0-900 ºC

Table 2. Thermocouple type available on *Gleeble* and its temperature range [35].

Once the sample´s surface oxide is removed by coarse polishing, thermocouples are weld to the sample in the central section where the temperature is to be controlled. The selected contact voltage for the welding process was $36V$. The thermocouple arrangement can be seen in figure 8. It is important to note that both welds are performed at the same transversal plane in order to avoid measurement problems related to applied current flowing through the thermocouples.

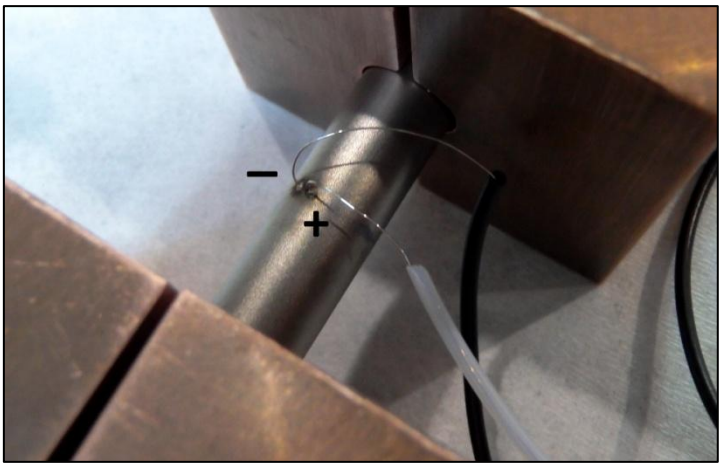

Figure 8. Thermocouple connection detail.

The processing of each sample is controlled with a software called QuikSim. This user-friendly interface enables a wide range of thermal and mechanical treatments by combining in time any of the capabilities offered by the *Gleeble*. The input window is shown in figure 9 as a practical example. A general cycle has been considered as an example to illustrate the procedure to give instructions to the machine.

	#	L	Time	Axis 1	Axis 2	Axis 3
1			System			
2			Stress-Strain	Axial strain using chStroke, l = 12mm, d = 10mm		
3			Acquire	Force PTemp Stroke TC4		
4			*			
5			*			
6			*			
7			Start	☑ Mechanical	☐ High	☑ Thermal
8			Mode	Force (kgf)	Wedge (cm)	TC4 (C)
9			Sample	10.0Hz		
10			00:05.0000	0.0	0.000	0
11			02:00.0000	0.0	0.000	1200
12			Zero	Stroke		
13			Mode	Stroke (mm)	Wedge (cm)	TC4 (C)
14			00:20.0000	0.00	0.000	1400
15			00:03.0000	0.00	0.000	1400
16			00:00.0005	0.00	0.000	0
17			00:00.1000	-12.00	0.000	0
18			Switch	Quench2	☑ On	
19			Sample	1000.0Hz		
20			00:03.0000	0.00	0.000	0
21			Switch	Quench2	☐ On	
22			00:00.1000	0.00	0.000	0
23			End	☐ Mechanical	☐ High	☐ Thermal

Figure 9. QuikSim cycle definition window.

The information in figure 9 should be read from the top to the bottom. The column of Time defines the instant at which a certain action takes place. The first instruction is to activate the mechanical and thermal capabilities. The machine will set the force and temperature to zero within 5 seconds before raising the sample's temperature to 1200ºC in 2 minutes, applying no force. Then, the elongation is constrained to zero (stroke mode) and the sample is

heated from 1200 to 1400ºC in 20 seconds. The temperature is maintained at 1400ºC for 3 seconds. Then heating is turned off (temperature set to zero). After 0.5 milliseconds, stroke begins. The achieved stroke is -12mm (compression) within 1 second. The quench is immediately turned on for 3 seconds, and finally the mechanical and thermal functions are deactivated.

Five samples have been successfully treated in the present work. The description of their processing, with both the programmed and real (measured) temperature evolution are shown hereafter.

- **3.2.1: Water quenched sample (WQ).** Heating at 10ºC/s up to 1400ºC. 3 seconds held at 1400ºC. Water quenching with a cooling rate of 26000ºC/s.

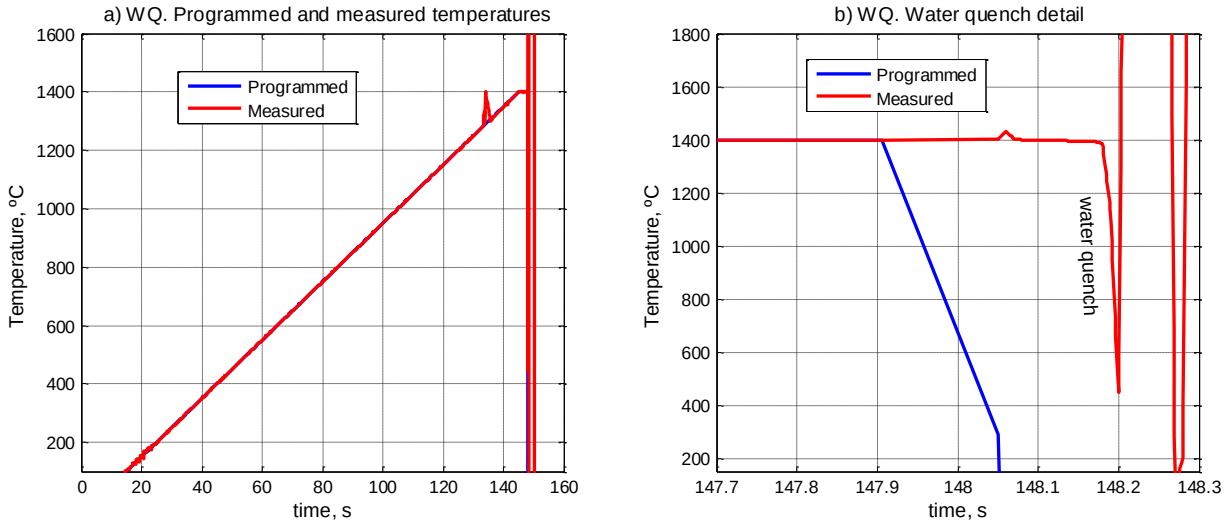

Figure 10. WQ temperature evolution, a) global cycle, b) detail.

It can be noticed that figure 10b) shows a very sharp temperature increase (followed by some high amplitude oscillation) right after water quench has cooled the piece. This is, of course, a wrong measurement coming from thermocouple detachment occurring at about 450ºC. By default, the temperature measured by the machine when thermocouples are not connected is 8000ºC.

- **3.2.2: Low cooling rate sample (LC).** Heating at 10ºC/s up to 1400ºC. 3 seconds standing at that temperature. Controlled cooling rate of 10ºC/s. This cycle is shown in figure 11.

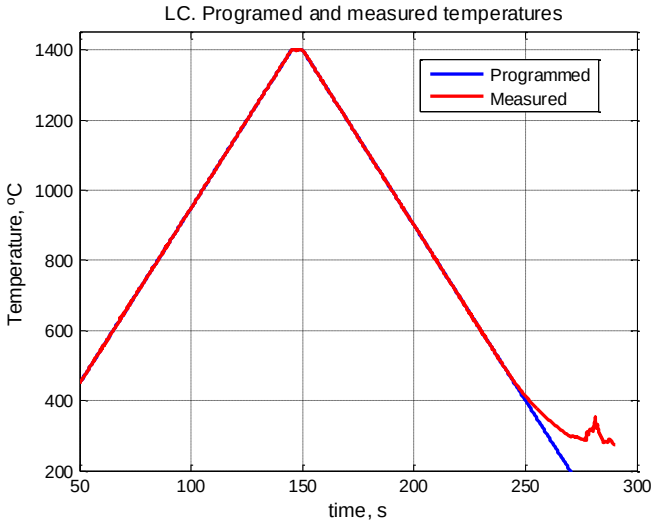

Figure 11. LC temperature evolution.

- **3.2.3: Very low cooling rate sample (VLC).** Heating at 10ºC/s up to 1400ºC. 3 seconds standing at that temperature. Controlled cooling rate of 1ºC/s.

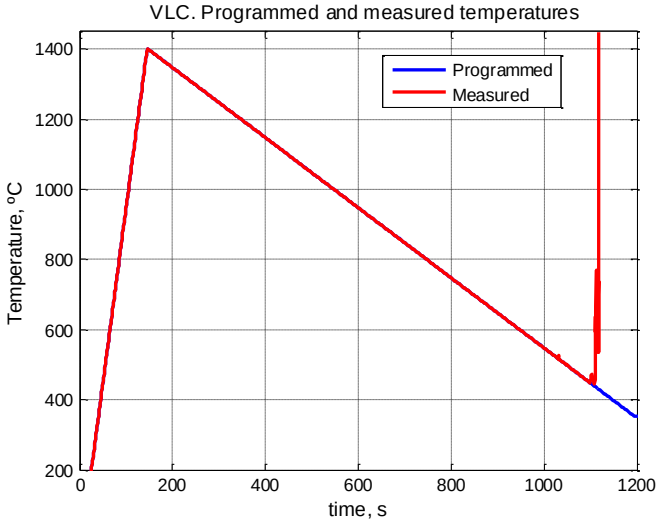

Figure 12. VLC temperature evolution.

Again, thermocouple detachment (temperature profile rising towards 8000ºC) can be observed in figure 12 at about 450ºC

The thermal cycles for both LC and VLC samples were performed at a vacuum of about $10^{-2}\mathrm{Pa}$ in order to minimize surface oxide formation during the relatively slow cooling.

- **3.2.4: Sample exposed to dynamic plastic deformation and water quenching (DPD).** Heating at 10ºC/s up to 1400ºC. 3 seconds standing at that temperature. Dynamic plastic deformation in compression with a reduction in length of 6mm achieved in 0.16 seconds. Water quenching

with a measured cooling rate of 3000ºC/s. The temperature evolution is shown in figure 13.

The engineering stress-strain curve (figure 14) has been obtained from the force (F) and elongation (Δl) on the specimen, which were directly provided by the *Gleeble*:

$$\sigma_{eng} = \frac{F}{A_0} \quad (1)$$

$$\varepsilon_{eng}\,(\%) = \frac{\Delta l}{l_0} 100 \quad (2)$$

Notice that compressive stress and elongations have been considered to be positive values. The interpretation of this plot is difficult since the temperature (and thus the mechanical properties) is varying through the test. However, the compression stage, between points A and C in the graph, does occur at a constant temperature of 1400ºC. The elastic behavior can be modeled with a straight line passing through points A and B with a Young modulus of $290.3\ \mathrm{MPa}$.

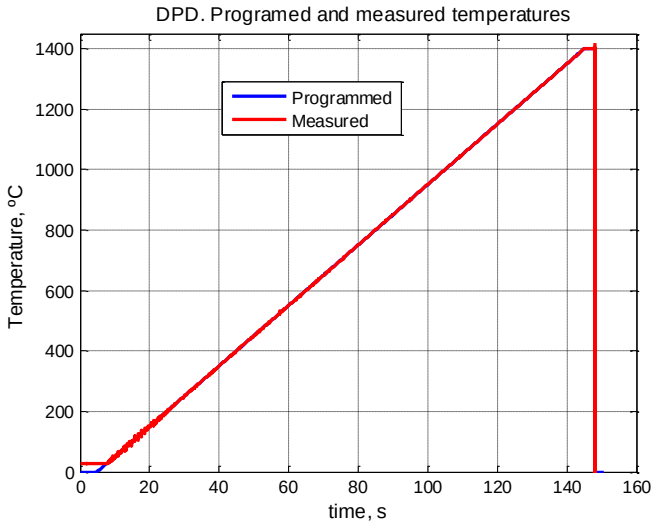

Figure 13. DPD temperature evolution.

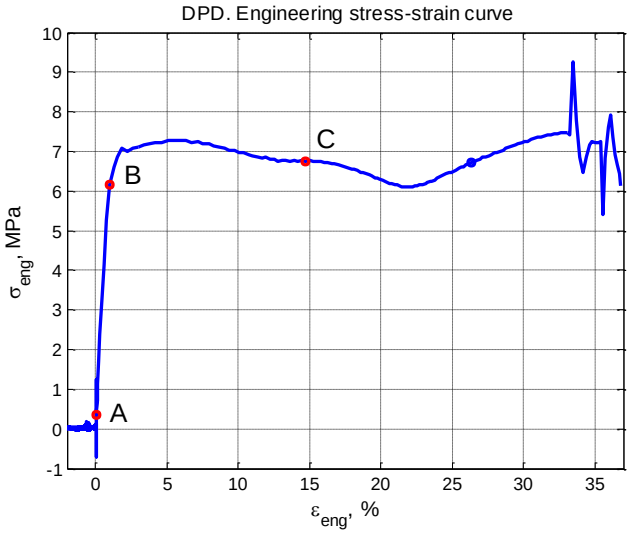

Figure 14. DPD engineering stress-strain curve.

- **3.2.5: Sample annealed before quenching with the water gun (AWQ).** Heating at 10ºC/S up to 1390ºC. Keeping at that temperature for 20 s (annealing). Water quench resulting in a cooling rate of 2000ºC/s. See this evolution in figures 15a) and 15b).

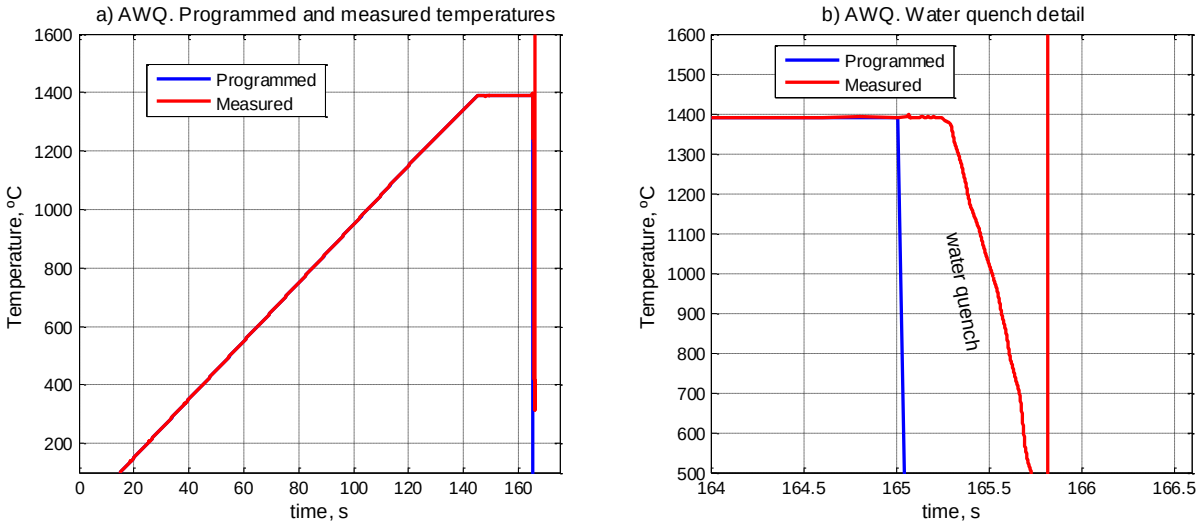

Figure 15. AWQ temperature evolution. a) global cycle, b) detail.

Obtaining specimens with dynamic plastic deformation followed by low cooling rates could not be achieved due to thermocouple detachment occurring at 1400ºC right before or during dynamic plastic deformation. The *Gleeble* machine is able to control the sample´s temperature by comparing the actual sample temperature with the programmed temperature. Based on their difference the machine will apply the required amount of power to minimize the error. Therefore if the measured temperature is wrong (when thermocouple detaches) the power input will as well be wrong causing an uncontrolled

temperature increase which lead to sudden sample melting. This phenomenon can be observed in figure 16.

Figure 16. Melted sample due to thermocouple detachment.

3.3 Sample preparation for microstructural characterization

Once the samples have been processed, the following operations are required to prepare them for the characterization stage. These post-processing techniques directly determine the quality of the results. They turn out to be, therefore, of vital importance for the development of this study.

First, the samples were cut-off with an alumina (Al_2O_3) disk at the sections of interest. For all samples but DPD, the section of interest coincides with the section were the *Gleeble* had a precise control, i.e. the centered transversal section. The DPD sample, however, was cut in a longitudinal plane enabling the analysis of microstructural gradients. The cutting machine utilized was a *Struers Accutom-5*.

In order to obtain an adequate surface finish for optical microscopy examination, the following sample preparation scheme was followed:

1. First, the samples to be prepared were mounted using a non-conductive resin. This was followed by manual grinding with decreasing roughness of the silicon carbide paper. 320, 600, 1200 and 2000 grit size *Struers* grinding paper were used. The large hardness difference between the samples and the epoxy resin used to mount it caused the formation of wear planes during manual grinding. Whenever this problem aroused, automatic rotation grinding was performed.

2. An automatic machine *Buehler Vector-Beta* was used to complete the mechanical polishing. See figure 17. The grinding cloths and diamond pastes used were $9\mu m$, $3\mu m$, $1\mu m$ and $0.04\mu m$.

Figure 17. Automatic polishing machine.

Before a sample was changed from one polishing stage to the following (finer) one, a thorough cleaning was carried out in order to avoid abrasive particles contamination between different stages. For this purpose the sample was introduced in ethanol and subjected to ultrasonic vibrations.

Electron backscatter diffraction (EBSD) examination required, additionally, a final electropolishing step in order to eliminate the remaining surface deformed layers. The machine used for this purpose was a *Struers LectroPol 5* electropolishing unit (figure 18). It is important to take into account that the electrolytical polishing procedure requires a fine ground surface to #1200 or finer [36]. This operation was performed at room temperature with the parameters in table 3, taken from [36]:

Electrolyte	A3
Temperature	~20ºC
Flow rate[1]	15
Voltage	40V
Time	25s

Table 3. Electropolishing parameters

Figure 18. Electropolishing equipment.

3.4 Microstructural characterization

[1] The units of the flow rate are not provided in electropolishing specifications.

- **3.4.1 Optical microscopy**

Microstructural characterization was initially carried out using an optical microscope *Olympus BX51*. This microscope is connected to a computer via *ColorView IIIu* digital camera. The microscope and the digital camera (on top of it) can be seen in figure 19.

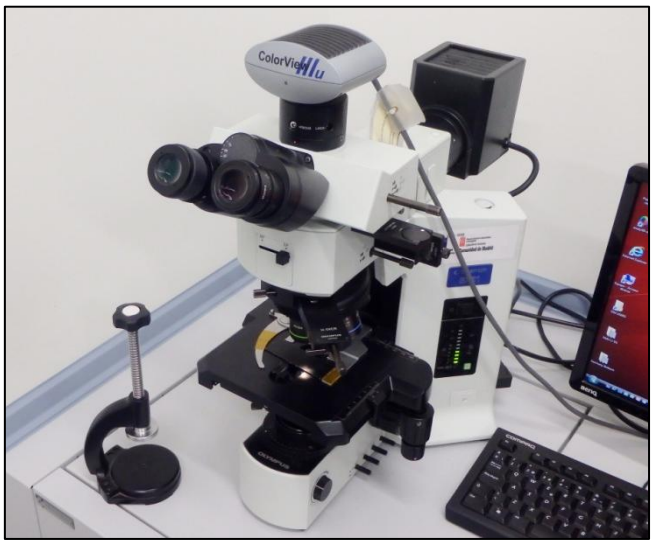

Figure 19. Optical microscope.

The distance between the objective and the surface of interest must be kept constant in order to achieve a well-focused image. With that purpose, the sample is placed on top of a small rounded clay portion and it is pressed with a manual clamp (low-left corner in figure 19) until the surface of the sample is parallel to the clamp surface. Thanks to the low elasticity of clay it is ensured that the sample remains its position during optical observation.

LC and VLC microstructures were appropriate for optical microscopy and important information could be extracted with this technique. However, grain boundaries of high cooling rate samples, WQ and DPD, could not be identified. Furthermore, phase distribution and orientation cannot be obtained through optical microscopy so these tasks are delegated to electron microscopy.

- **3.4.2 Scanning electron microscopy**

The scanning electron microscope (SEM) (figure 20) and, in particular, the EBSD technique, have been essential tools for the characterization of TiAl samples. Once the samples surface is appropriate, the specimens are introduced in the SEM following the steps described below:

- Fix sample to pin. Electrical conductivity between the sample and the pin must be enhanced to ensure electron flow and avoid local surface charging. The fixing methods consisted on using a double-face adhesive

graphite band, *loctite* adhesive (non conductive) with silver coating, or any combination of them.

- Fix pin to 70º pre-tilt support.
- Mount support on SEM stage. The support must be oriented so that the surface of interest points towards the EBSD detector.
- Vacuum the chamber. This is essential for the operation of the electron beam to be efficient.

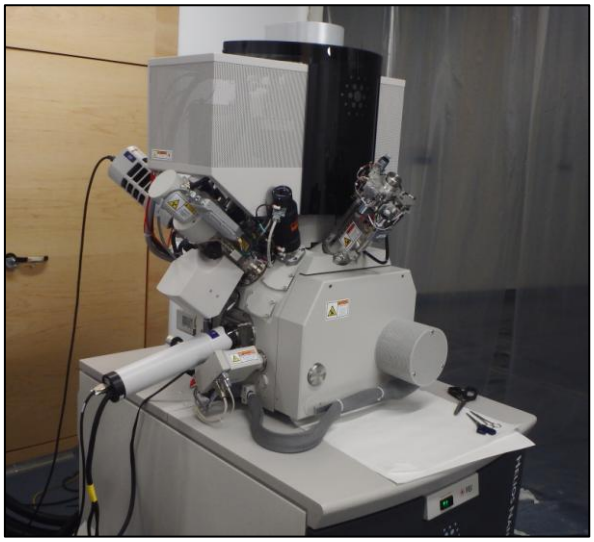

Figure 20. Dual beam SEM at *IMDEA*.

The SEM principle is to emit a focused electron beam towards a point of the sample and acquire information by analyzing the corresponding diffracted electron beam. The imaging of a sample is achieved, then, by scanning its surface and by acquiring information for equidistant points in a given area. The resolution of the image depends, then, on the size of the electron probe, which is directly related to the energy of that beam (its accelerating voltage). Depending on the information to be extracted, different detectors for the different types of diffracted electrons can be used.

In particular the technique of electron backscatter diffraction (EBSD) utilizes the information of the group of diffracted electrons that have fulfilled Bragg's law, and that are emitted from the sample, which is tilted 70°, along the surface of cones of very large aperture:

$$n\lambda = 2dSin\theta$$

Where n is an integer, λ is the wavelength of the electron beam, d is the interplanar spacing for the considered crystallographic plane and θ is the angle at which electrons diffract (relative to the crystallographic plane) when Bragg´s law is satisfied.

The projection of these high aperture cones on a phosphor screen (electron sensitive) gives rise to an arrangement of lines that are known as

Kikuchi bands (see figure 21), and which form the so-called Kikuchi patterns. The interpretation of these patterns, together with a database of crystallographic information for different materials, enables the identification of the phases and their orientation. An introductory explanation of the fundamentals of EBSD can be found in [37].

A huge difference was observed in the Kikuchi patterns of the electropolished and the non electropolished specimens. This comparison can be clearly seen in figure 21.

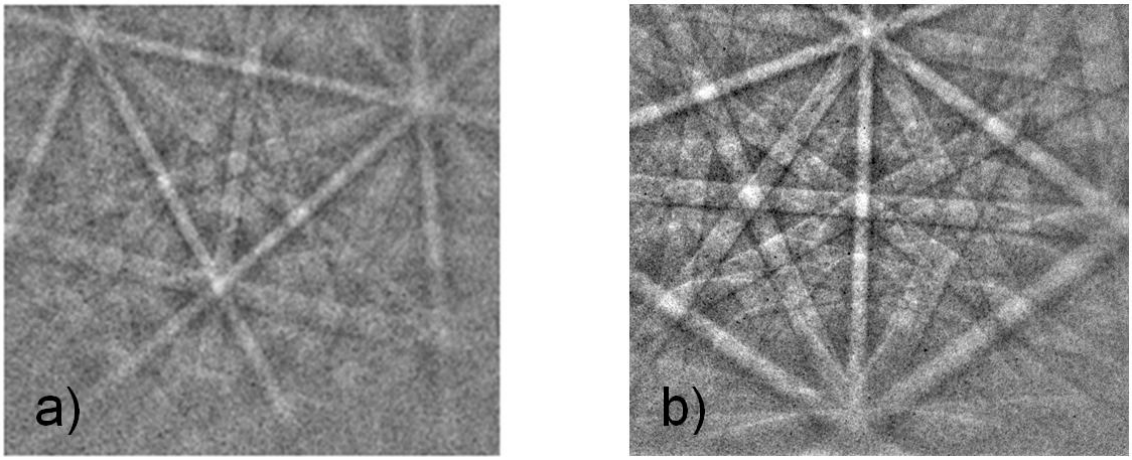

Figure 21. Kikuchi pattern for a) mechanically polished and b) electropolished samples.

- **3.4.3 Transmission electron microscopy**

Transmission electron microscopy (TEM) was utilized to determine the crystal structure of the phases present in the processed specimens and, in particular, to distinguish between the α_2 and α phases. Although both possess hexagonal structures, the appearance (or not) of superlattice spots in the selected area diffraction (SAD) pattern corresponding to the <0001> zone axis allows to determine whether the α_2 phase is present (or not). In order to facilitate the alignment of the <0001> zone axis perpendicular to the sample surface, focused ion beam micromachining was utilized to cut a lamella with a suitable orientation. The procedure consisted on the steps that are described below.

The specimen to be analyzed by TEM must be thin enough so that a parallel electron beam can be transmitted through it. First, EBSD enabled the identification of the region of the material with the appropriate lattice orientation and the focused ion beam (FIB), then, was used to extract the thin lamella at that particular location. A detailed explanation of the lamella extraction procedure can be found in section 3.6.3.

The desired relative orientation between the hexagonal cell and the lamella plane is plotted schematically in figure 22.

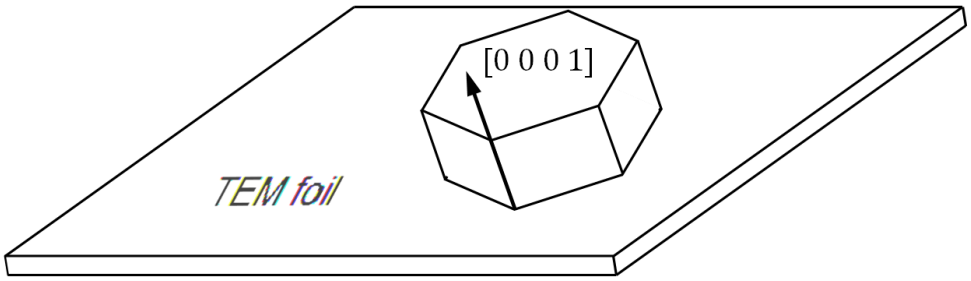

Figure 22. Desired lamella-crystal relative orientation

3.5 Microhardness

The microhardness of the samples was measured using a microhardness Vickers indenter (*Shimadzu HMV-2*) (figure 23). A minimum of 10 indentations were performed in each sample in order for the measurements to have statistical significance.

Figure 23. Microhardness indenter.

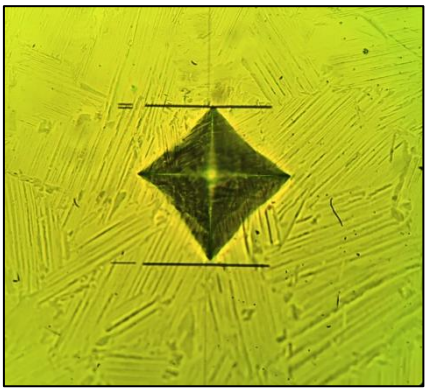

Figure 24. Vickers indentation on lamellar microstructure.

3.6 Other experimental procedures

- **3.6.1 Calculation of the colony size by the linear intercept method**

The linear intercept method has been applied to estimate the colony size of the lamellar microstructures. Several straight lines are drawn in the optical micrograph and the number of cuts with the grain boundaries is counted. In order to avoid wrong measurements in case some preferred direction for grain growth existed, six lines have been drawn radially from the centre of the image with a separation of 60º. See figure 25 as an example. The average colony size is then found with the following formula:

$$Size = \frac{cuts}{length} 1.7 \qquad (3)$$

Where $length$ is the sum of the length of the drawn lines and the factor 1.7 takes into account that 2D measurements are used to calculate what is in reality a 3D feature.

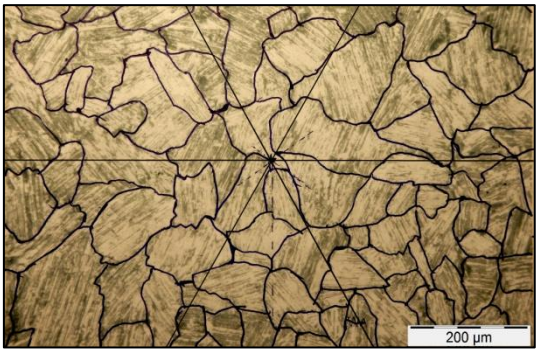

Figure 25. Hand-drawn colony boundaries and straight lines for linear intercept method

- **3.6.2 Lamellae width computation**

For γ-TiAl lamellar microstructures, the determination of the lamellae width distribution cannot be directly drawn from the measurement of the thickness of

each of the bands observed in an Inverse Pole Figure (IPF) contrast EBSD map. A correction must be applied to take into account that the angle formed between the lamellae interfaces and the mapped surface, θ, will not be exactly 90º in a general case. Being θ different for each colony. See the volume of figure 26 to better understand this problem:

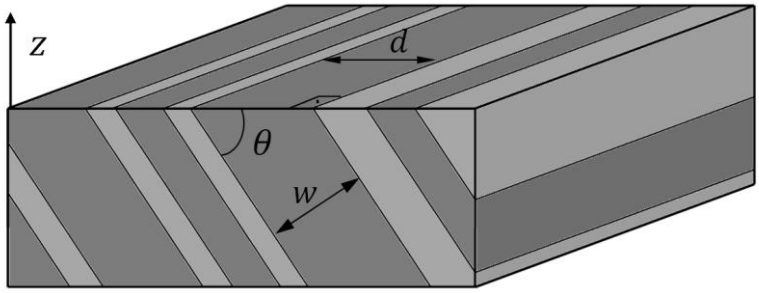

Figure 26. Spatial distribution of lamellae in a colony.

where the relation between d and w is given by:

$$w = d\ sin(\theta) \tag{4}$$

The thickness values obtained from the electron-imaged surface, d, can be measured directly for each of the lamellae in a IPF contrast EBSD map. However, finding the true lamellae width, w, requires the computation of θ taking into account crystallographic aspects of this particular alloy. The orientation of a lamella with respect to the surface can be obtained from its Euler angles if and only if the relative orientation between that crystal and the interfaces between adjacent lamellae is known. This information is indeed given by the Blackburn relationship for γ-TiAl lamellar intermetallics (see expressions 5 and 6, taken from [38]) which constraints the spatial orientation of the crystals inside a γ or α_2 lamella with the following conditions:

- The basal plane of HCP α_2 phase is parallel to the lamellar interfaces.
- One of the {1 1 1} planes in a γ plate is parallel to the lamellar interfaces, allowing defined rotations of 60º about its normal vector giving rise to 3 possible configurations.

$$\{111\}\,\gamma \,||\, \{0001\}\,\alpha_2 \tag{5}$$

$$<110>\,\gamma \;||\; <11\text{-}20>\,\alpha_2 \tag{6}$$

Any of these constraints can be used to determine θ, being the first one much clear since it directly imposes the scalar product condition:

$$\cos\theta = \frac{\boldsymbol{z_h}\cdot\boldsymbol{z}}{|z_h||z|} \tag{7}$$

Where $\boldsymbol{z}$ is the vector normal to the sample surface (0,0,1) and $\boldsymbol{z_h}$ is the normal direction to the (0 0 0 1) plane in the hexagonal cell of a particular α_2 lamella, given in the sample coordinate system.

In order to obtain the normal direction to the (0 0 0 1) plane in the global sample reference frame, its Euler angles are required. This information is contained in the EBSD map data and can be acquired with the software *Channel5*. For the particular sample reference system selected during acquisition of the map, the rotation matrix, G, allows the determination of $\boldsymbol{z_h}$ through the Euler angles of a particular crystal given by φ_1, ϕ, φ_2.

$$G = \begin{bmatrix} g_{11} & g_{12} & g_{13} \\ g_{21} & g_{22} & g_{23} \\ g_{31} & g_{32} & g_{33} \end{bmatrix} \quad (8)$$

$$g_{11} = cos(\Phi_1) \cdot cos(\Phi_2) - sin(\Phi_1) \cdot sin(\Phi_2) \cdot cos(\phi); \quad (9)$$
$$g_{12} = sin(\Phi_1) \cdot cos(\Phi_2) + cos(\Phi_1) \cdot sin(\Phi_2) \cdot cos(\phi); \quad (10)$$
$$g_{13} = sin(\Phi_2) \cdot sin(\phi); \quad (11)$$
$$g_{21} = -cos(\Phi_1) \cdot sin(\Phi_2) - sin(\Phi_1) \cdot cos(\Phi_2) \cdot cos(\phi); \quad (12)$$
$$g_{22} = -sin(\Phi_1) \cdot sin(\Phi_2) + cos(\Phi_1) \cdot cos(\Phi_2) \cdot cos(\phi); \quad (13)$$
$$g_{23} = cos(\Phi_2) \cdot sin(\phi); \quad (14)$$
$$g_{31} = sin(\Phi_1) \cdot sin(\phi); \quad (15)$$
$$g_{32} = -cos(\Phi_1) \cdot sin(\phi); \quad (16)$$
$$g_{33} = cos(\phi); \quad (17)$$

Then, the obtention of $\boldsymbol{z_h}$ is simply applying:

$$\boldsymbol{z_h} = \boldsymbol{G^{-1}} \cdot \boldsymbol{c} \quad (18)$$

Where $\boldsymbol{c}$ are the local Cartesian coordinates of the normal to the (0 0 0 1) plane:

$$c = (0,0,1) \quad (19)$$

For this, a *Matlab* code has been developed in order to calculate the relative angle between the lamellae and the surface given the Euler angles for a hexagonal crystal, taken with *Channel5*, as input data.

- **3.6.3 Lamella extraction procedure**

Figure 27 shows the different steps performed with the FIB in order to obtain a lamella for TEM observation.

First, the surface of interest was protected with a platinum coating (figure 27a). This deposition is achieved by localizing a platinum cloud close to the surface of interest and enhancing its accumulation in the surface with the appropriate ion beam intensity per unit area. Too much intensity would result in a degradation of the surface aimed to be protected while a low value will not be

sufficient for platinum deposition process to start. The required value for the FIB intensity was $6\ \mathrm{pA}/\mu\mathrm{m}^2$.

The next step is known as FIB milling. It is observed in figures 27b) to 27d). An intensity of $21\mathrm{nA}$ and a voltage of $30\mathrm{kv}$ were the selected parameters to perform this operation. The final size of the lamella strongly depends on the depth reached with this abrasive process. It can be noticed how platinum coating acts as a barrier to Ga^+ impact and therefore reduces its milling capacity.

Once enough depth is reached during milling, it is necessary to reduce the thickness of the lamella to electron transparency. The first part of the thickness-reduction process is shown in figure 27e) and 27f).

Then, the lamella is separated from the bulk by cutting all but one of its edges. At this state, the lamella is welded to a manipulation needle with platinum deposition. Once it is fixed to the needle, its last connecting edge to the bulk can be removed and the lamella can be gently extracted with the needle. The lamella is then fixed to the grid that will be placed on the TEM holder. Figure 28 shows a lamella welded to the needle and to the grid for TEM examination [39].

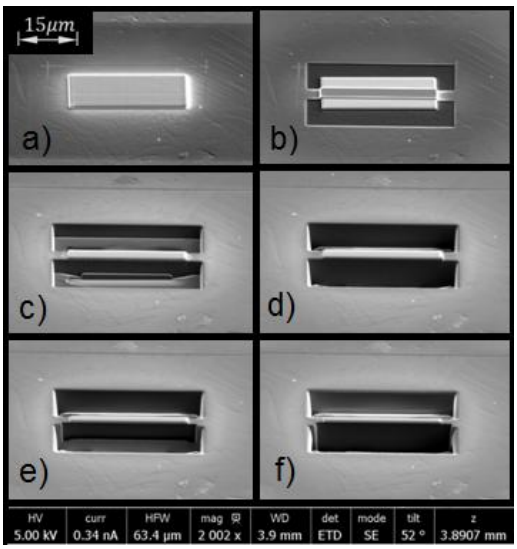

Figure 27. Different stages in the obtention of a lamella for TEM.

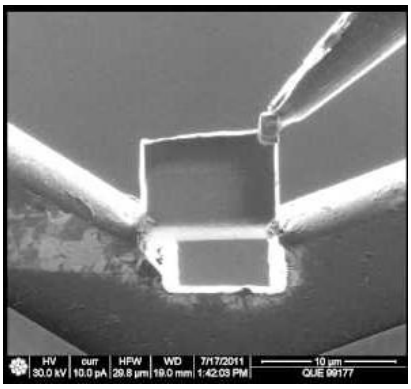

Figure 28. Lamella welded to needle and TEM support [39]

Once the lamella is attached to the grid, further material removal was performed. The current for this final operation, known as FIB cleaning, was $2.5\ \mathrm{nA}$. This current is smaller than that used during FIB milling in order to minimize Ga^{+} implantation on the final observation surface. The process finishes when a thickness of about $100\ \mathrm{nm}$ was achieved.

More detailed information regarding TEM sample preparation with FIB can be found in [40].

- **3.6.4 Sample preservation**

In order to minimize surface quality deterioration whenever the samples were not analyzed or manipulated during long periods of time, a small vacuum chamber was used to keep them isolated from air. It is formed by two hemispherical pieces of plastic that achieve a hermetic seal when they are properly arranged and connected to a vacuum supply. See figure 29.

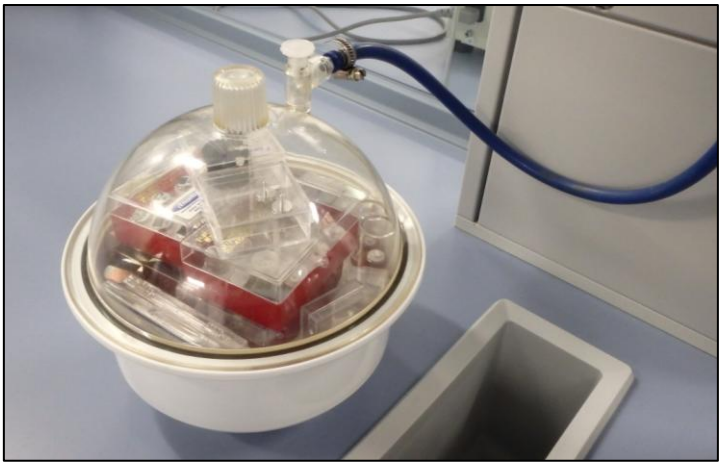

Figure 29. Vacuum chamber.

4. Results and discussion

The results shown here have been grouped individually for each of the samples in order to assess the effect of each of the processing treatments alone. Afterwards, a general perspective has been considered by comparing all the samples in order to determine which one exhibits the best mechanical behavior.

4.1 As-received material

- **4.1.1 Microstructure**

Optical microscopy has been used to determine the appearance of the microstructure of the as-received material. As can be seen in figure 30, the microstructure is fully lamellar. This is a typical microstructure of the $\mathrm{Ti4522XD}$ in the as-cast condition [25]. Colonies exceeding $100\ \mu\mathrm{m}$ in size are populated with alternating lamella of the α_2 and γ phases.

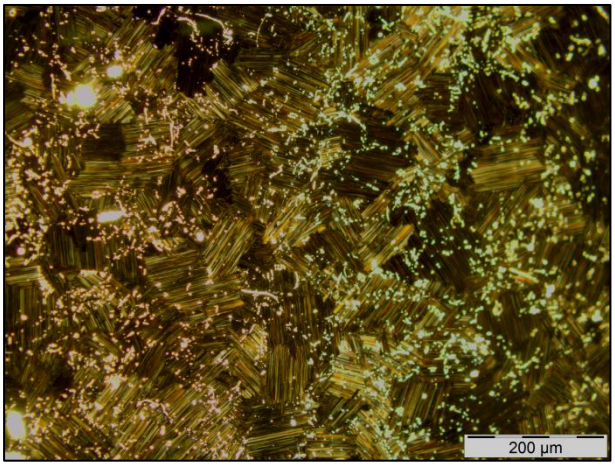

Figure 30. Microstructure of the as-received material.

- **4.1.2 Hardness**

Ten Vickers indentations were performed in random locations of the sample. The average HV hardness was found to be 301 with a normalized standard deviation (coefficient of variation[2]) of 5%.

[2] The coefficient of variation is defined as the standard deviation over the mean. It is useful to assess the measurement's quality of sampling.

4.2 Water quenched sample (WQ)

- **4.2.1 Macroscopic defects**

A Y-shaped crack developed at the centre of the WQ specimen as shown in figure 31. This means that internal thermal stresses above the yield point of the material[3] developed during the fast water quench cooling.

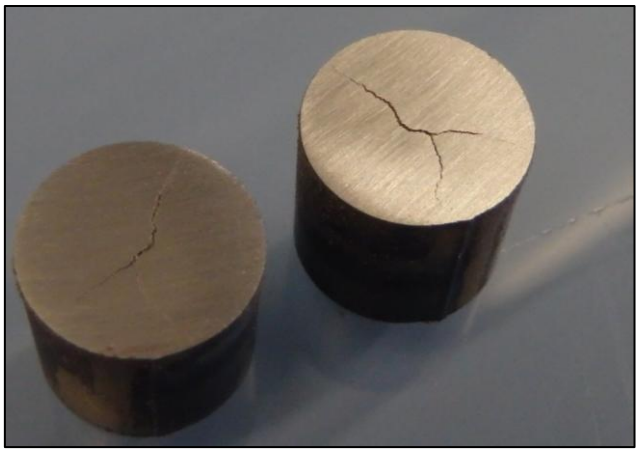

Figure 31. Crack in WQ sample.

- **4.2.2 Microstructure**

In order to investigate the presence of microstructural gradients due to cooling-rate variations throughout the sample, several EBSD maps were obtained at different locations of a sample. The location of the maps in the cross section of the WQ sample is identified with a number as can be observed in figure 32. Locations 1, 3 and 4 are in the peripheral region of the transversal observation plane. Location 2 corresponds to the centre of the specimen.

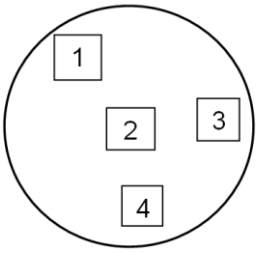

Figure 32. Location of each map in WQ sample.

[3] The yield point of the material depends on temperature and the temperature(s) at which the crack developed is not known.

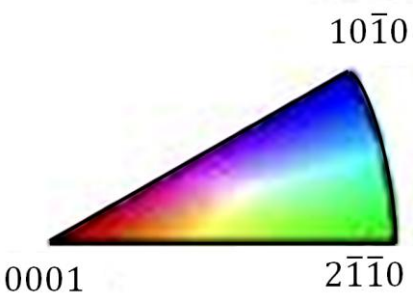

Figure 33. IPF-Z color scale for α_2 phase.

The EBSD orientation maps (left) and phase contrast maps (right) for each of these locations can be seen in figures 33-37. Fig. 33 is the color legend corresponding to the normal direction for α_2 phase in the orientation maps. In the phase contrast maps, the blue color is the γ phase and the red one is a hexagonal phase that could be α or α_2. The EBSD technique does not allow distinguishing between these two phases since the mean angular deviation (MAD) between the experimental Kikuchi bands and the theoretical phase model is very similar when any of the two phases (α_2 and α) are considered. Thus, TEM examination has been carried out in order to determine the exact nature of the hexagonal phase (see below).

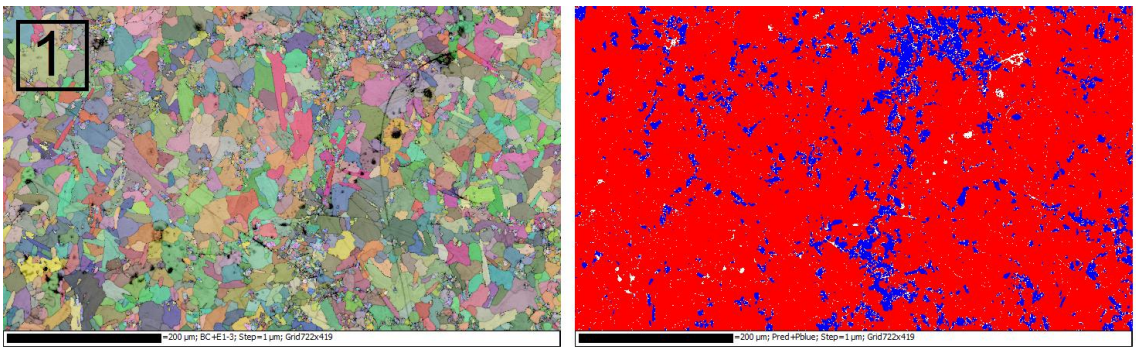

Figure 34. Orientation (left) and phase contrast (right) maps at location 1.

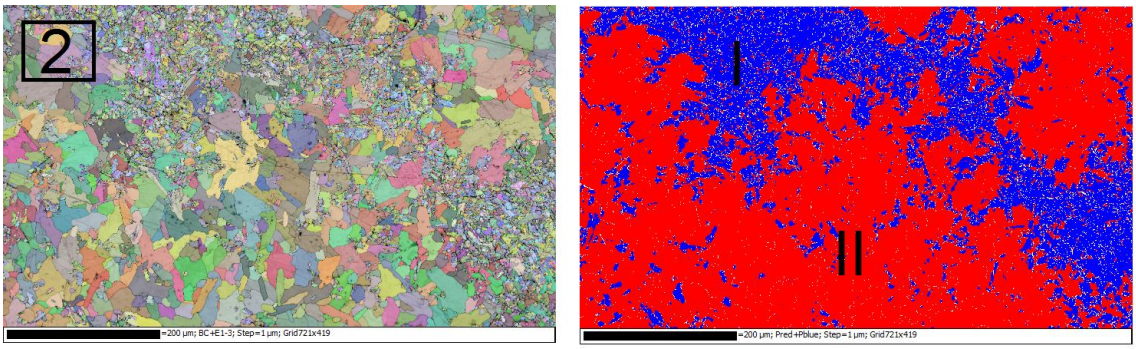

Figure 35. Orientation (left) and phase contrast (right) maps at location 2.

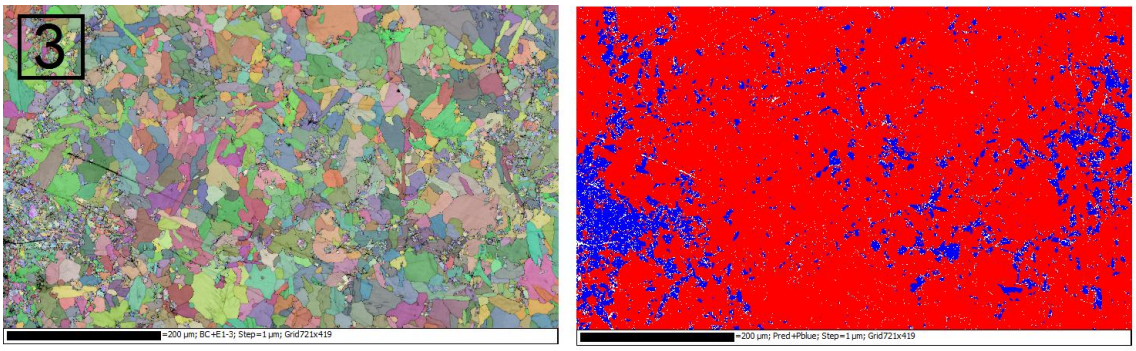

Figure 36. Orientation (left) and phase contrast (right) maps at location 3.

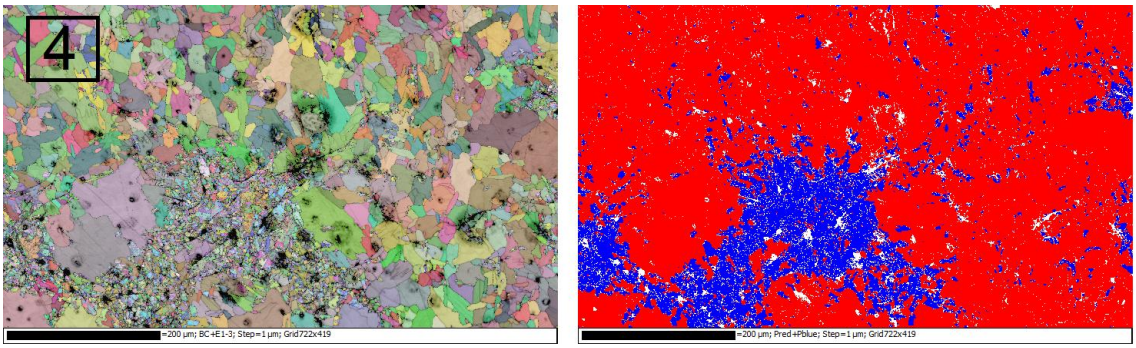

Figure 37. Orientation (left) and phase contrast (right) maps at location 4.

The phase distribution in this sample is very heterogeneous, irrespective of the location. In some regions there is a high concentration of small γ grains and a very low content of small α (α_2) grains (see region I in figure 35). Other regions are mainly composed of relatively large α_2 grains with a low concentration of small γ grains (see region II in figure 35). The map at the centre (location 2) reveals a 29% of area of γ phase. The average γ phase content at the exterior locations is 13%. In the three maps performed close to the perimeter, the γ phase concentration seems to be a repeatable (non casual) result. This difference in gamma phase content might be explained by the occurrence of non-uniform cooling rates in the sample. Since the water quench jet directly impinges on the surface of the specimen, greater cooling rates are expected there. In fact, the cooling rates measured during sample processing were those at the surface of the specimen, were thermocouples were welded. According to this explanation, the presence of γ phase is enhanced with lower cooling rates.

According to the binary $TiAl$ phase diagram (figure 2) the alloy considered in this study (45%Al) becomes single phased at temperatures above 1300ºC. However (assuming a diffusion process), some time is required for the

'low' temperature phases (α_2 and γ) to transform into α phase. Therefore it could be possible that some of the γ phase in the WQ sample could be there simply because it didn´t have time to transform to the high temperature stable α phase during the 3 seconds kept at 1400ºC (see WQ processing in section 3.2). In order to validate this idea, it was deemed necessary to process another sample (AWQ) with the same cooling rate than WQ but with more time maintained above the α transus line. The microstructure and properties of this sample will be detailed below (section 4.6).

Other phenomena that should be taken into account when analyzing the microstructural results are the potential thermal gradients during heating at a constant temperature. Since the specimen is heated in the *Gleeble* via the Joule effect and heat losses occur through the surface, there exists a steady-state temperature gradient when the specimen is kept at a constant temperature. This temperature gradient (i.e. the difference between the center and the surface temperatures) will depend on the thermal resistance of the material and the surrounding atmosphere. To have an idea of the stent of this gradient, the graph in figure 38 has been found in [35].

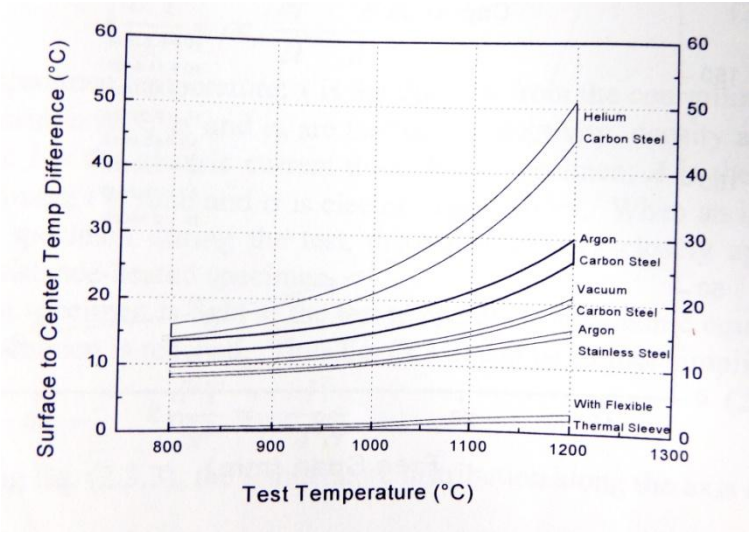

Figure 38. Temperature difference between the centre of the specimen in different environments.

The conditions in this study can be approximated to that of carbon steel surrounded with argon at a test temperature of 1200ºC. Therefore the approximate temperature difference between the surface and the centre is about 30ºC. Probably this is not enough to contribute to significant microstructural changes but in any case it is important to bear it in mind.

The sample is formed by grains of irregular shape. The grain size has only been obtained for α (α_2) phase since it is the most abundant phase in this sample. Furthermore, the detection of γ grains was problematic due to the

presence of pseudosymmetries[4] in this phase. For the detection of grains the software *Channel5* has been used. Only grains separated by a boundary with misorientation above 15º and a size above $5\,\mu m$ in equivalent diameter have been considered. The mean value of α (α_2) grains in the centre (location 2), calculated with *Matlab* from the EBSD map data, is $10\,\mu m$. The mean value of α_2 grains in all the maps close to the surface is $12\,\mu m$. The grain size histograms for the central map and the maps close to the surface are shown in figures 39 and 40, respectively. Notice that the y-axis of this histogram is not the number of grains but the area occupied by each group of grains with respect to the total map area (in %). In that way it is ensured that if a very large grain existed covering most of the map, it would not be just a small bar with a value of one. Therefore this histogram is an area-weighted grain size histogram.

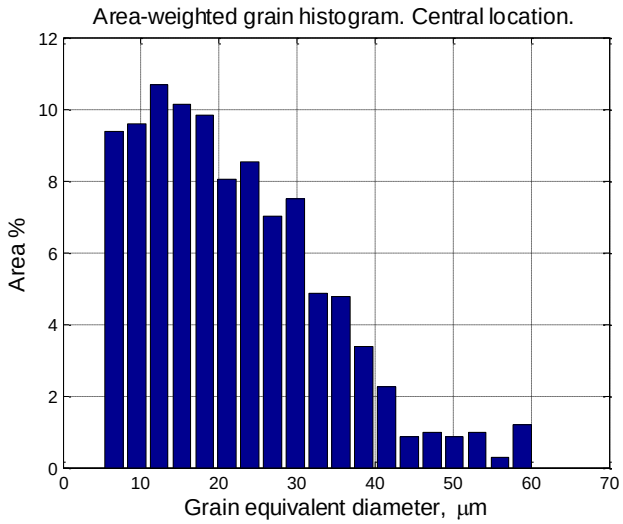

Figure 39. Central map α_2 grain size histogram.

[4] The unit cell of the γ phase has a tetragonal structure, with the height greater than width (section **1.2**) by a factor of about 1.02. The pseudo-symmetry problem occurs because the EBSD patterns corresponding to several orientations of this lattice are very similar and the software might not be able to distinguish between them.

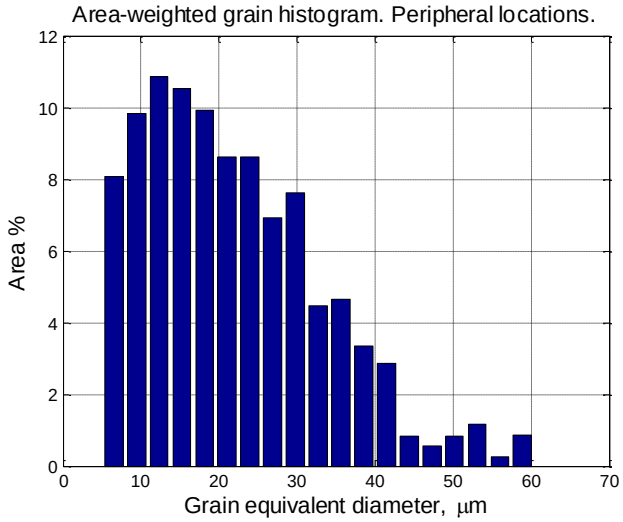

Figure 40. Surface locations α_2 grain size histogram.

These histograms resemble a normal (Gaussian) distribution. The area-weighted mean grain size (M_A) can be as well computed:

$$M_A = \frac{\sum_i^{end} A_i \cdot G_i}{A} \quad (20)$$

Where A_i is the area of each grain, G_i is the size of each grain, A is the total area of all the grains and end is the total number of grains. With this method, the mean grain sizes are $22\ \mu m$ at the centre and close to the surface respectively. This value is larger than the conventional mean calculation (equation 21) since larger grains have a greater weight in the calculation as they occupy more area.

$$M = \frac{\sum_i^{end} G_i}{end} \quad (21)$$

As explained in the processing section, the high cooling rates achieved with the *Gleeble* in the WQ sample have never been utilized before to process the $Ti4522XD$ alloy. Thus, a description of the resulting phases could not be found in the literature. In order to determine the exact nature of the hexagonal phase (α_2 or α), TEM examination and, in particular, selected area diffraction (SAD), of the WQ sample was carried out. α_2-Ti_3Al is an intermetallic where the aluminum atoms always occupy the same position in the repeating unit cell. However, the α phase is ideally composed of only Ti atoms and the presence of Al is as solid solution, with no order. The procedure required to achieve these patterns is described in section 3.4.3. The SAD pattern in figure 41 corresponds to the basal zone axis of the WQ sample. Two kinds of spots can be distinguished. Weak spots correspond to superlattice diffractions that are characteristic of ordered structures. This proves that the hexagonal phase detected by EBSD was, indeed, the intermetallic α_2.

Figure 41. TEM SAD diffraction pattern along the basal zone axis in the WQ sample.

- **4.2.3 Hardness**

Vickers hardness has been measured at the center and peripheral regions of the sample. Ten indentations were performed at each of these locations. In the central part, the average hardness was found to be 463 with a coefficient of variation of 4.6%. Close to the surface, the average hardness was found to be 470 with a coefficient of variation of 2.6% (standard deviation over mean value). The variation of the hardness between the centre and the exterior of the sample is only of 1.5%. This is consistent with the presence, in both cases, of a large fraction of α_2 phase with similar grain size.

4.3 Low cooling rate sample (LC)

- **4.3.1 Microstructure**

The microstructure of the low cooling rate sample, LC (10ºC/s), is illustrated in the optical micrograph of figure 42. This image was taken in dark field mode at a magnification of x200. The image reveals a fully lamellar microstructure, which is to be expected given the cooling rate utilized [29].

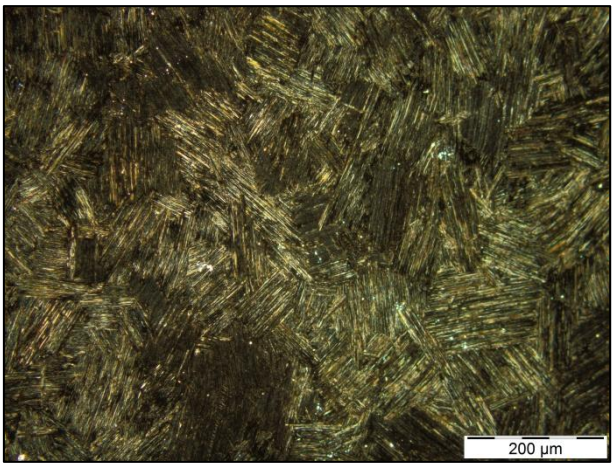

Figure 42. LC microstructure at x200.

The mean lamellar colony size has been calculated using the linear intercept method (see section 3.6.1). It has been found to be $94\,\mu m$ in equivalent diameter.

EBSD was used to analyze in greater detail the lamellar microstructure. As expected, the lamellar microstructure is an arrangement of the two phases γ-$TiAl$ and α_2-Ti_3Al. The EBSD phase contrast map for the LC sample is shown in figure 43. The reason why the aspect ratio of this map is exaggerated (very long and narrow rectangle) is that this is the best shape in order to maximize the number of lamellae captured in the map (to achieve statistical validity) while minimizing the total acquisition time, thus avoiding detrimental drifting effects. Drift is the uncontrolled deviation of the electron beam from its ideal path. Charge drift was one of the greatest problems when capturing EBSD maps since it can result in wrong measurements of lamellae width. The reason why charge drift occurs is the local charge accumulation on the surface due to scarce electric conductivity (electron flow). These effects can be mitigated by enlarging the step size, since the beam focuses at fewer points within the scanned area. This results in a lower surface intensity in $A/\mu m^2$, and thus fewer electrons are to be evacuated per unit surface. The main drawbacks of increasing the step size are lower map resolution (fewer pixels for the same area) together with a lower capability to detect the thinnest lamellae. The step size for EBSD mapping was set to $0.065\,\mu m$. This value was the largest one that still ensured the capability to identify lamellae. Drift was also mitigated by reducing the exposure time to acquire Kikuchi patterns at each point. Even with these particular settings, some drift was still present in the maps. Notice how the lamellae interfaces in the phase contrast map are not completely parallel to the band contrast background in figure 43. The average lamellae width for γ and α_2 phases has been found to be 0.17 and $0.04\ \mu m$ respectively. The average lamellae width has been found to be $0.12\,\mu m$. See section 3.6.2 to understand the computation of the lamellae width.

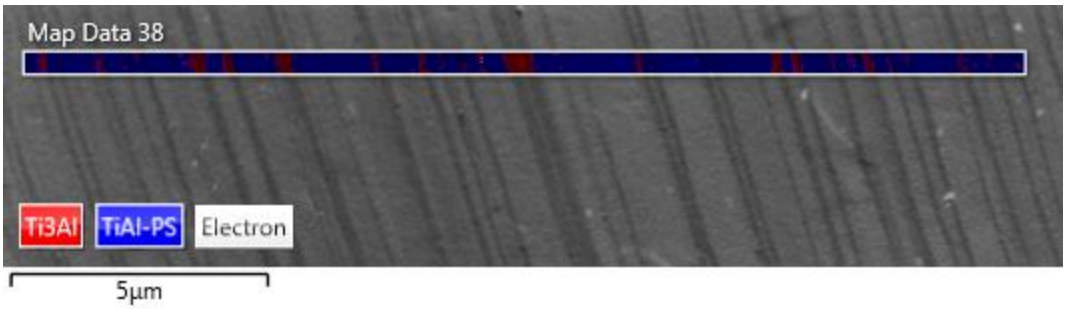

Figure 43. LC EBSD phase contrast map over SEM band contrast image. Phase α_2 is in red and phase γ in blue.

The distribution of the sampled lamellae widths can be observed in figure 44. For each of the phases this distribution seems to be normal with all values centered about the average width mentioned earlier.

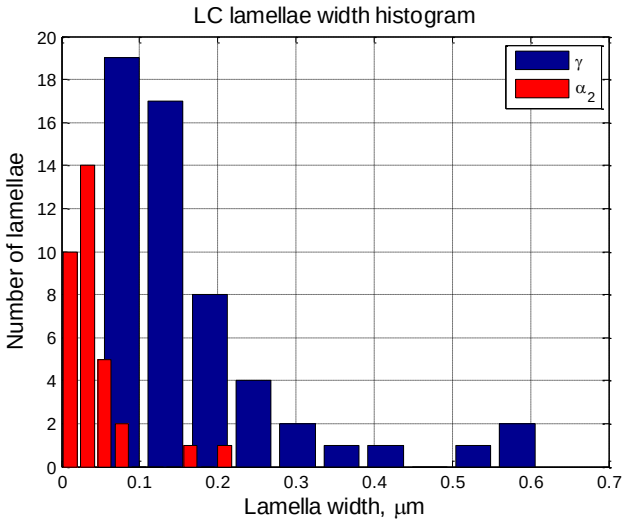

Figure 44. Lamellae width histogram for each phase in LC sample.

Based on the information from several EBSD maps, the phase content of each sample has been found to be 88 % of γ for LC. It should be born in mind that the thinnest lamellae could not be detected by EBSD.

- **4.3.2 Hardness**

The Vickers microhardness of LC sample was found to be 367 in mean value, with a coefficient of variation of 3.7%. To achieve these results, ten indentations were performed.

4.4 Very low cooling rate sample (VLC).

- **4.4.1 Microstructure**

With the optical microscope, the microstructure of the very low cooling rate sample, VLC (1ºC/s), has been found to be fully lamellar as observed in figure 45. This image was taken in dark field mode at a magnification of x200. This result is expected since a cooling rate of only 1ºC/s ensures thermodynamic equilibrium transformations that correspond to lamellar microstructure in γ-TiAl alloys [29].

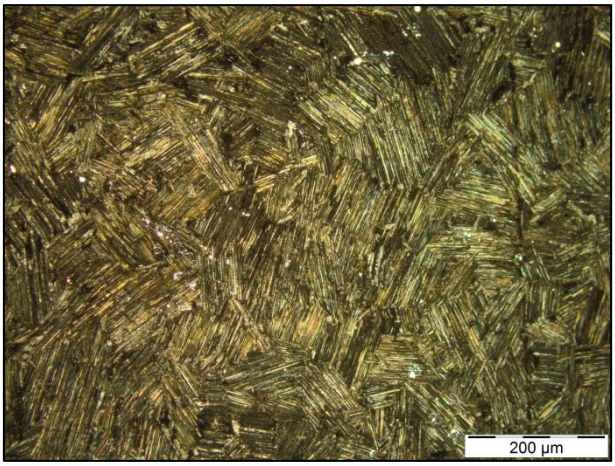

Figure 45. VLC microstructure at x200.

The mean lamellar colony size has been calculated using the linear intercept method (see section 3.6.1). It has been found to be $103\,\mu m$ in equivalent diameter.

The EBSD map were the lamellae width information was extracted is shown in figure 46. In the VLC sample, the average lamellae width for the γ and α_2 phases has been found to be 0.42 and $0.16\,\mu m$ respectively. The average lamellae width has been found to be $0.29\,\mu m$. See section 3.6.2 to understand the computation of the lamellae width.

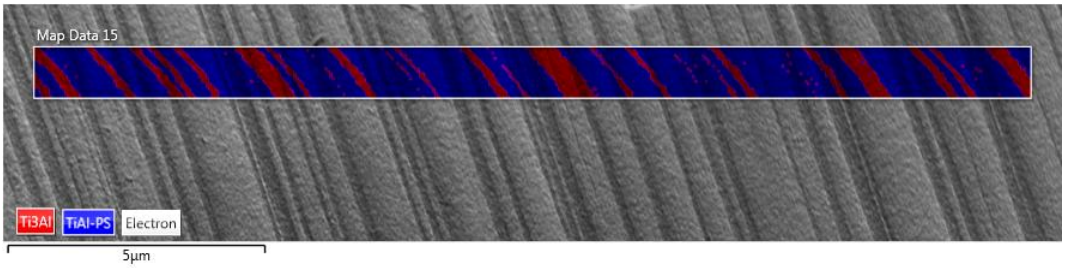

Figure 46. VLC EBSD phase contrast map over SEM band contrast image.

The distribution of the sampled lamellae widths can be observed for both phases in figure 47. Notice that this distribution does not have the appearance of a normal distribution meaning that there could be a wider range of preferable width values in comparison with the centered distribution of LC sample (figure 45).

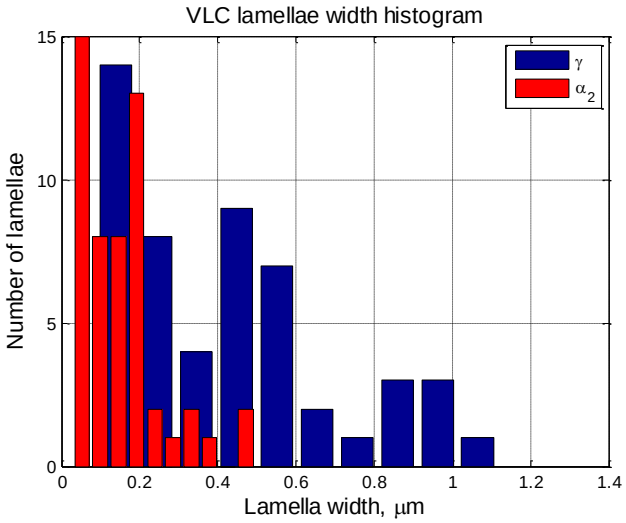

Figure 47. Lamellae width histogram for each phase in VLC sample.

- **4.4.2 Hardness**

Vickers hardness has been measured with ten indentations. The mean value resulted in 317 and the coefficient of variation was 4.6%.

4.5 Sample exposed to dynamic plastic deformation and water quenching (DPD).

- **4.5.1 Macroscopic defects**

The 6 mm compressive elongation at high temperature, together with the high cooling rate associated to quenching, caused the sample to fracture and gave rise to a very irregular and rough fracture surface. A longitudinal straight crack also developed. These macroscopic features can be observed in figure 48, where the fracture surface (transversal plane) of DPD sample is shown.

Figure 48. Fracture surface of DPD sample.

- **4.5.2 Microstructure**

The EBSD grain orientation maps and the phase contrast maps corresponding to three different locations (Figure 49) can be observed in figures 50-52. Two regions (1 and 2) have been examined within the plastically deformed area. One additional region (3) outside such area has also been analyzed.

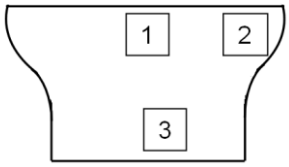

Figure 49. Location of each examined region in DPD sample (longitudinal section).

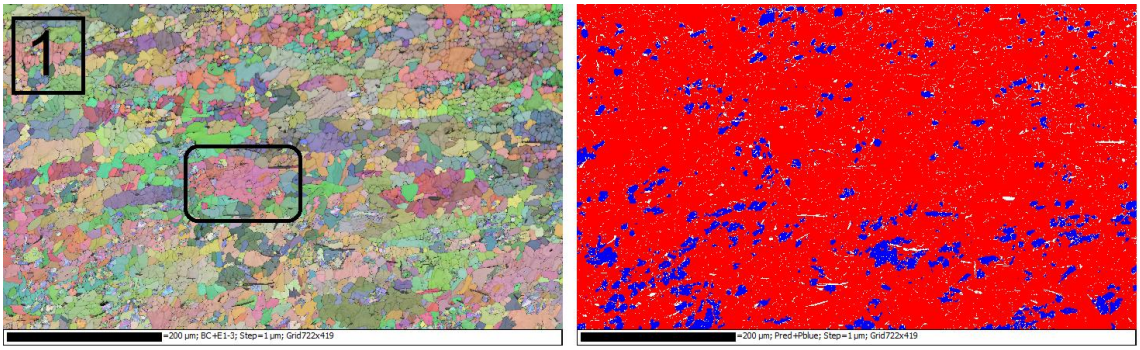

Figure 50. Orientation (left) and phase contrast (right) EBSD maps at location 1.

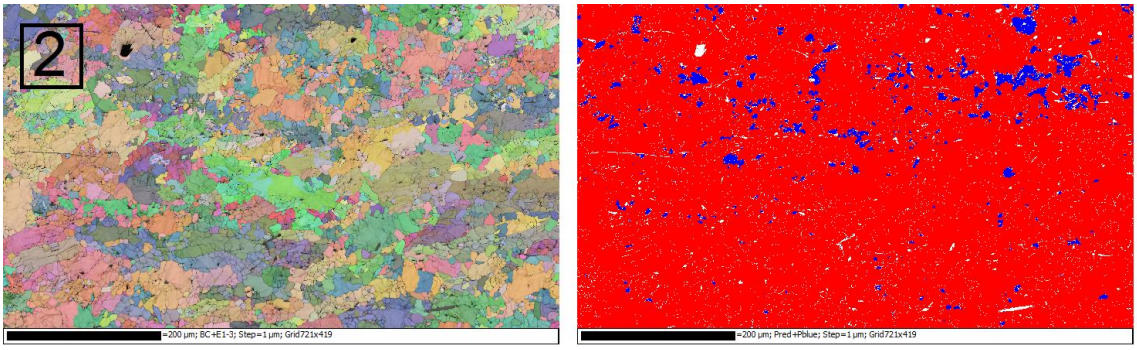

Figure 51. Orientation (left) and phase contrast (right) EBSD maps at location 2.

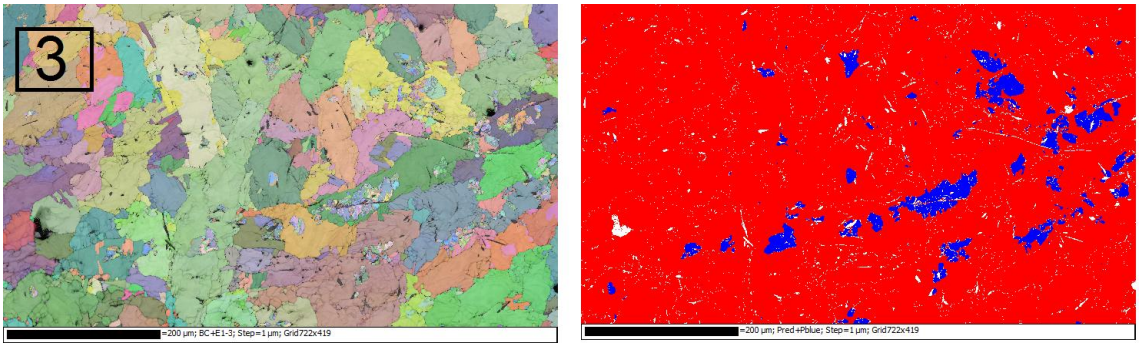

Figure 52. Orientation (left) and phase contrast (right) EBSD maps at location 3.

The color legend corresponding to the normal direction for α_2 phase in the orientation maps can be seen in Fig. 33. In the phase contrast map, the blue color is γ phase and the red one is α (α_2). The distribution of the two phases in the DPD sample is more homogeneous than in the WQ sample. γ grains are clearly identifiable and are dispersed within the hexagonal matrix.

An obvious effect of the applied deformation at high temperature is grain refinement. By simple visual inspection of the maps it can be observed that the grains in location 3, separated from the barreled region, are much larger than in locations 1 and 2, where dynamic plastic deformation has occurred.

Another effect of plastic deformation is the appearance of subgrains. This can be clearly observed in figure 53, a zoom-in of the circled region in figure 50, where a grain containing multiple subgrains is shown. The crystal lattices in these subgrains have similar orientations (approximately the same color) but low angle boundaries have developed due to dislocation rearrangement promoted by the need to minimize energy [41].

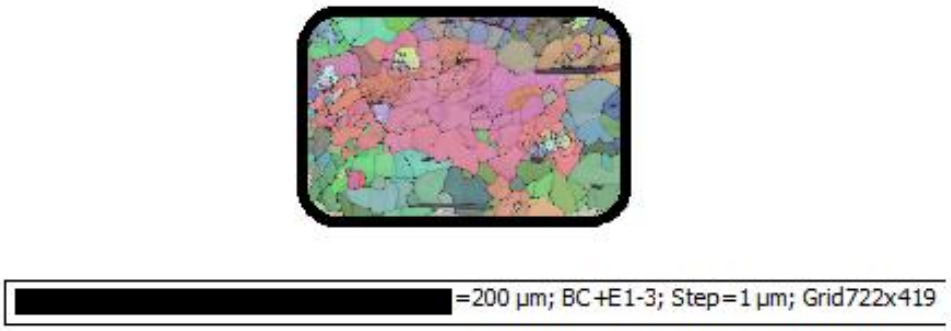

Figure 53. Grain (purple) with visible subgrains.

The phase volume fraction is very similar in all the maps and has a mean value of 91% in α (α_2) for the whole sample. In the central location the content of γ is slightly larger than the mean resulting in a volume fraction of 88% in α (α_2). This variation would match with lower cooling rates achieved in the centre, but the difference in γ phase content is too small to ensure it.

The grain size histogram illustrated in figure 54 groups the grains from locations 1 and 2, while the grain size distribution in location 3 is shown in figure 55. The mean area-weighted grain size is $25\ \mu m$ for the maps were deformation occurred (locations 1 and 2). The mean grain size at location 3 is $33\ \mu m$. This value is a 34% larger than the mean grain size at the deformed locations, proving the grain refinement caused by deformation. It can be noticed that grains below $10\ \mu m$ in size occupy the largest area fraction. However, a wide dispersion of grain sizes is actually present.

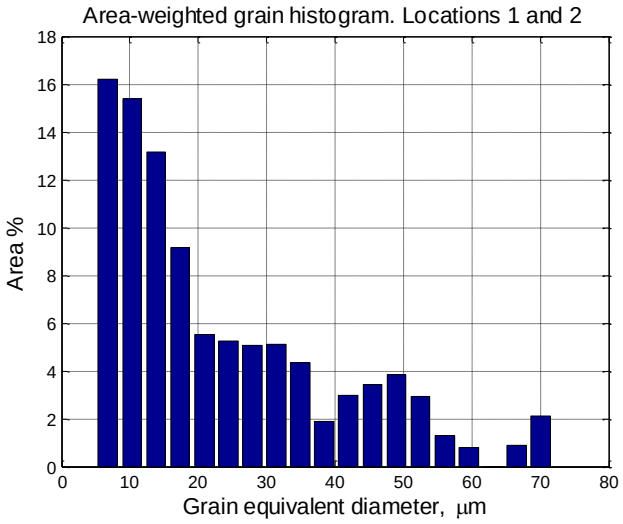

Figure 54. α (α_2) grain size histogram.

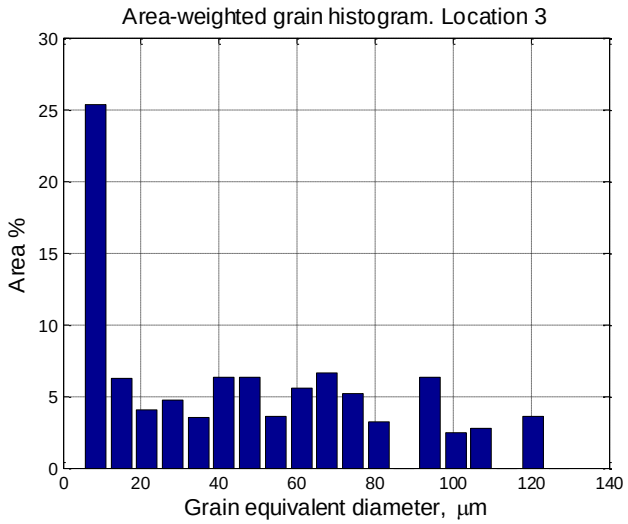

Figure 55. α (α_2) grain size histogram.

The TEM SAD diffraction pattern for DPD sample can be observed in figure 56. Here, too, superlattice spots (smaller) can be observed, confirming that the hexagonal phase is the intermetallic α_2. The reason why the repeating distribution of spots in this pattern has a different arrangement than in WQ diffraction pattern (figure 41) is that the zone axis, in this case, is a prismatic direction, and not a basal direction.

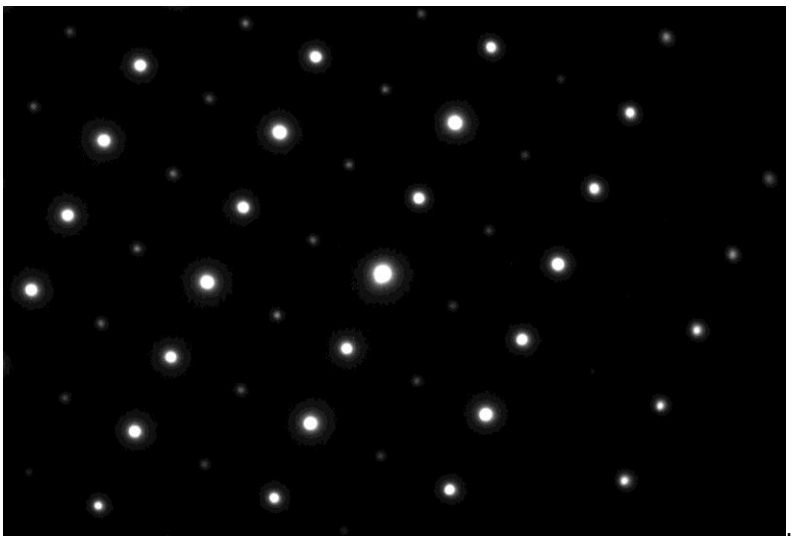

Figure 56. TEM diffraction pattern in DPD sample.

- **4.5.3 Hardness**

The Vickers hardness at the deformed section of the sample has been found to be 478. This result is only a 2.5% larger than the WQ sample hardness. It cannot be ensured, therefore, that this dynamic process at high temperature does improve the mechanical properties with respect to the WQ processing.

4.6 Sample annealed before quenching with the water gun (AWQ).

- **4.6.1 Macroscopic defects**

As well as in WQ sample, a Y-shaped crack developed in the centre of AWQ specimen (figure 57). The sample in this figure is shown after electropolishing. Similar internal stresses as in WQ sample seem to have developed as a consequence of the extreme cooling rates associated to quenching.

Figure 57. Macroscopic crack in the AWQ sample.

- **4.6.2 Microstructure**
  The locations examined in the AWQ sample are shown in figure 58.

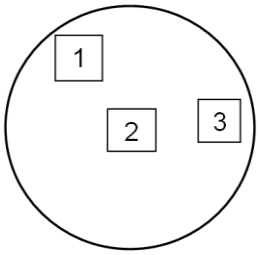

Figure 58. Location of the examined regions in the AWQ sample.

The EBSD maps acquired at the different locations of the AWQ sample are depicted in figures 59-61, the orientation map being at the left and the phase contrast map at the right of each figure. The most surprising result is the absolute lack of γ phase in map 2, taken at the centre of the sample. The magnification of these maps is x150. This is a low value, taking into account that a modern SEM can reach magnifications above x500000 [42]. A significant portion of the surface of the sample is being observed. This ensures results to be reproducible in space. 0% of γ in map 2 is a key result to determine the conditions that constrain the formation of γ-TiAl phase. At the peripheral locations (1 and 3), the volume fraction of γ is approximately 31%.

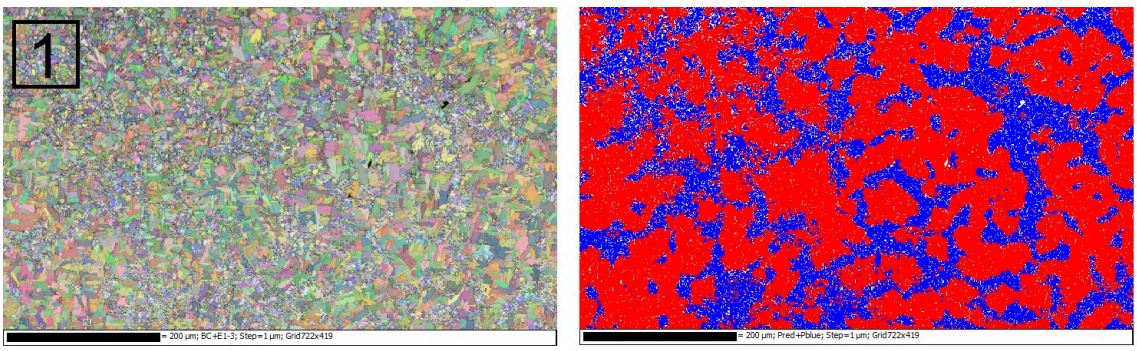

Figure 59. Orientation (left) and phase contrast (right) maps at location 1.

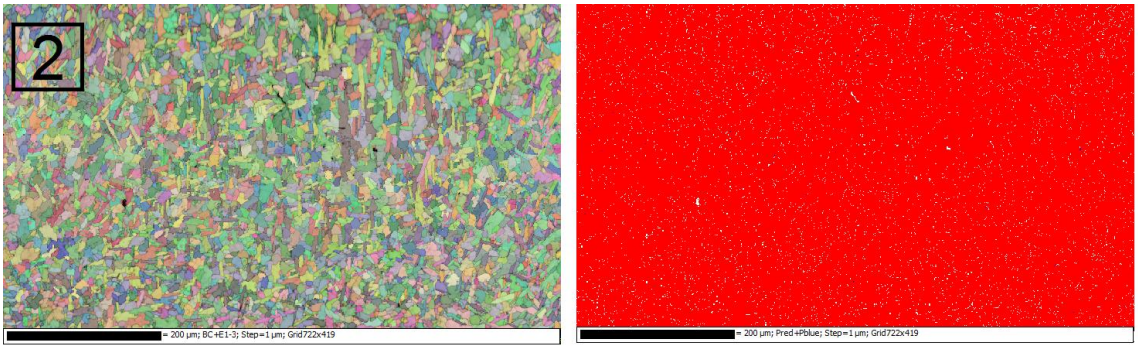

Figure 60. Orientation (left) and phase contrast (right) maps at location 2.

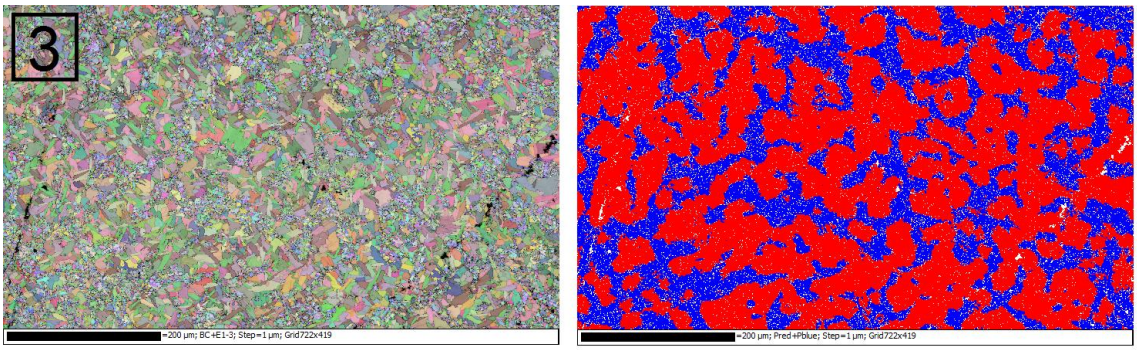

Figure 61. Orientation (left) and phase contrast (right) maps at location 3.

The mean grain size of the α (α_2) phase, calculated using equation 21, is $14\ \mu m$ both at the centre (2) and at the surface locations (1 and 3). It was unfortunately not possible, due to time constraints, to determine whether the hexagonal phase present in AWQ sample is α_2 or α phase.

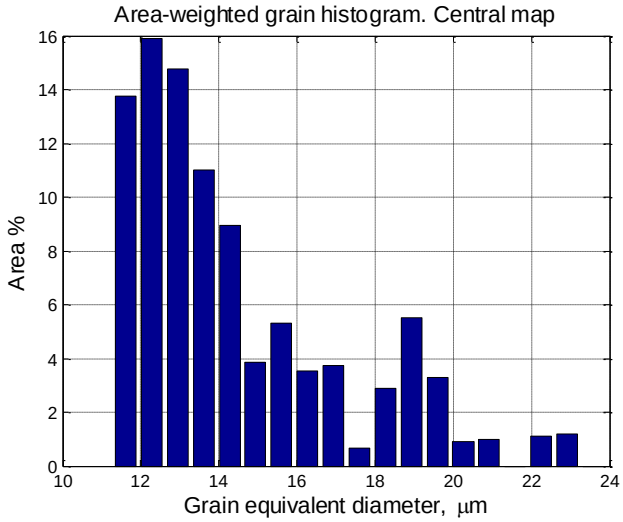

Figure 62. AWQ α (α_2) grain size histogram.

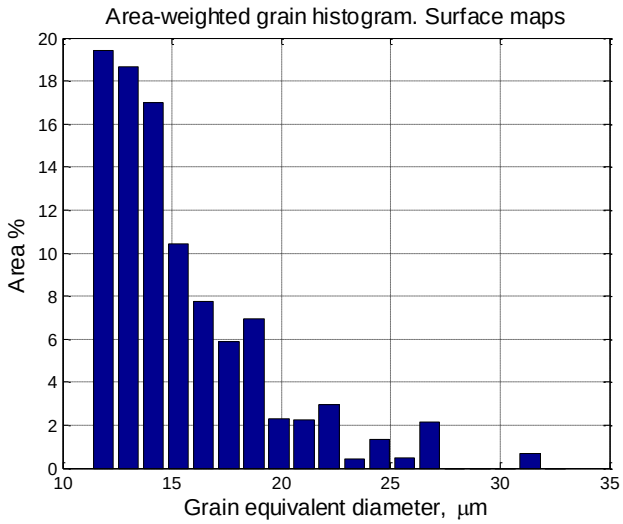

Figure 63. AWQ α_2 grain size histogram.

- **4.6.3 Hardness**

The hardness measurements have provided very promising results. First, the average hardness of the whole sample was calculated. With this aim, a total of 22 indentations were performed at random locations. The mean Vickers hardness obtained was 506, with a coefficient of variation of 3.3%. Then, the hardness of the surface and the central regions were estimated separately. Ten indentations were performed on each region in order to achieve this goal. The mean hardness close to the surface was found to be 488, with a coefficient of variation of 2.9%; the mean hardness at the centre was found to be 532, with a coefficient of variation of 1.7%.

4.7 Outlook

Table 4 summarizes the main microstructural characteristics and the hardness values obtained for all the samples analyzed in the frame of the present project.

Sample	Mean HV	Structure	Phases
As-received	301	lamellar	-
WQ	464	equiaxial	α_2(80%) + γ(20%)
LC	367	lamellar	α_2(12%) + γ(88%)
VLC	317	lamellar	α_2(24%) + γ(76%)
DPD	477	equiaxial	α_2(91%) + γ(9%)
AWQ (centre)	488	equiaxial	α (α_2)
AWQ (peripheral)	532	equiaxial	α (α_2)(69%) + γ(31%)

Table 4. Mean Vickers hardness and microstructure for each of the samples.

In the current literature it is considered that two-phase titanium aluminide alloys and, in particular, lamellar microstructures, exhibit a much better mechanical performance than their monolithic constituents γ-TiAl and α_2-Ti_3Al and that duplex or equiaxed gamma structures [43]. The results obtained in the current project reveal, however, that, single-phase α (α_2) Ti4522XD, obtained by rapid quenching from the α phase using a *Gleeble* system, can exhibit a significantly larger strength than lamellar microstructures of the same alloy. Although further work needs still to be carried out in order to elucidate the origin of the extraordinary hardness values achieved, as well as the structure of the hexagonal phase in the AWQ sample, the results obtained in this project will undoubtedly pave the way to develop novel processing routes for gamma Ti-Al alloys.

A note must be made here that the macroscopic defects (sections 4.2.1, 4.5.1 and 4.6.1) inherent to very high cooling rate processing, however, could deteriorate macroscopic performance of the material in terms of strength, creep resistance or fracture toughness. Thus, further work needs to be carried out also in this direction in order to minimize the appearance of such defects.

Table 5 compares the average colony size and lamellae width corresponding to the LC and VLC samples, both of which exhibit lamellar microstructures. It can be seen that increasing the cooling rate does not have a strong influence on the average colony size but it does result in a significant reduction of the lamellae width, leading to a significant increase of the hardness (Table 4). Due to the complexity of the microstructures of gamma TiAl alloys, which are governed by a large number of parameters (colony size, lamellae width, phase composition, volume fraction of equiaxed γ grains, fraction of lamella interfaces, etc), it is extremely difficult to isolate the influence of a specific microstructural feature. The results obtained in this project indicate that, at least when using cooling rates between 1 and 10$℃/s$, samples can be

developed in which the effect of the colony size could be isolated from the influence of other parameters, thus providing guidelines for microstructural design in these materials. Further work needs to also be carried out in order to evaluate the misorientation of the lamellae in LC and VLC samples.

Specimen	**Cooling rate** $^{\circ}C/s$	**Average colony size (μm)**	**Average lamellae width (μm)**
LC	10	94	0.12
VLC	1	103	0.29

Table 5. Values for colony size and lamellae width in LC and VLC samples.

5. Conclusions

In the present project the gamma TiAl alloy Ti4522XD was processed by different routes using *Gleeble* technology in order to explore the possibility to develop advanced microstructures with enhanced mechanical behavior. In particular, several samples of this material were held for 3 to 20 seconds within the alpha phase region and then cooled using cooling rates ranging from 1 °C/s to as high as 20000 °C/s; an additional sample was deformed within the single phase region and then quenched. The main conclusions obtained are summarized below.

1. Cooling rates below 10°C/s give rise to lamellar microstructures, formed by colonies populated with alternating layers of the γ and α_2 phases. Within this range of cooling rates the average colony size is not very influenced by cooling rate, but the lamellae width is observed to decrease with increasing cooling rate.

2. Quenching from the alpha phase after 3 seconds at high temperature, both with and without dynamic plastic deformation at such temperature, results in a microstructure in which the main constituent is the α_2 phase. The morphology of the α_2 grains is rather irregular, but mostly equiaxed. Grain size is a function of the applied strain, and subgrains are observed when deformation at high temperature is applied. Quenched samples have higher hardness than the lamellar microstructures obtained at lower cooling rates.

3. Increasing the holding time within the alpha phase region to 20 seconds, followed by rapid quenching, results in a microstructure in which, at least in the center regions, no gamma phase was detected. This microstructure has extraordinary hardness values.

6. Future work

Very promising results have been obtained in the current project, which call for a wealth of further work and open new avenues for the development of advanced gamma TiAl alloys. A list of topics for future research is shown below.

1. Analysis by transmission electron microscopy of the crystal structure of the hexagonal phase resulting from the AWQ process. This phase exhibits very high hardness values and, thus, must be analyzed in depth. Selected area diffraction patterns along the basal zone axis should be obtained in order to detect the possible appearance of superlattice spots, which would be indicative of order and, therefore, of the presence of the α_2 phase.

2. Mechanical testing of the AWQ sample and, in particular, of the center regions, where no gamma phase was detected, in order to determine the main deformation mechanisms at a wide range of temperatures and strain rates. Tests could be, first, performed in miniaturized specimens, machined from the mentioned center regions, by conventional uniaxial testing machines. Furthermore, micromechanical tests could also be carried out by milling micropillars at the areas of interest using a focused ion beam and then compressing them using nanoindentation at a wide range of temperatures.

3. Further optimization of the processing parameters in order to, first, avoid the formation of cracks during quenching and, second, to explore the possibility to form even stronger microstructures. In particular, the effect of longer times at temperature within the single-phase alpha region could be investigated.

7. References

[1] G. Sauthoff, *Intermetallics*, 1995, VCH, New York.
[2] K.J. Hemker and W.D. Nix. *Structural Intermetallics*, 1997, TMS, Warrendale, PA, p. 21.
[3] N.S. Stoloff, V.K. Sikka, eds. *Physical metallurgy and Processing of Intermetallic Compounds*. 1996. Chapman & Hall, New York.
[4] J.H. Westbrook and R.L. Fleischer, eds. *Structural Applications of Intermetallic Compounds*, 2000, Wiley, New York.
[5] R.W. Cahn, *Mater. Sci. Eng. A* 324 (2002) 1.
[6] O. Izumi, *Mater Trans JIM* 30 (1989) 627.
[7] M. Yamaguchi and Y. Umakoshi, *Prog. Mater. Sci.* 34 (1990) 1.
[8] S.C. Deevi, V.K. Sikka, and C.T. Liu, *Prog. Mater. Sci.* 42 (1997) 177.
[9] J.H. Westbrook and R.L. Fleischer, eds. *Basic Mechanical Properties and Lattice Defects of Intermetellic Compounds*, 2000, Wiley, New York.
[10] P. Veyssière, *Mater. Sci. Eng. A* 309-310 (2001) 44.
[11] M. Yamaguchi, H. Inui, and K. Ito, *Acta mater*. 48 (2000) 307.
[12] H. Oikawa, T.G. Langdon, *Creep Behavior of Crystalline Solids*,B. Wilshire, R.W. Evans, eds., 1985, Pineridge, Swansea, UK, p. 33.
[13] F.R.N. Nabarro and H.L. de Villiers, *The Physics of Creep*, 1995, Taylor & Francis, Bristol.
[14] D. Shah and E. Lee. J.H. Westbrook, *Intermetallic Compounds*, R.L. Fleischer, ed., 2002, Vol. 3, John Wiley &Sons, Chichester, UK, p. 297.
[15] J.H. Schneibel and P.M. Hazzledine, *Applied Sciences* 213 (1992) 565.
[16] R.E. Smallman, T.S. Rong, and I.P. Jones. *The Johannes Weertman Symposium,* 1996, TMS, Warrendale, PA, p. 11.
[17] G. Sauthoff, *Structural Intermetallics*, 1993, TMS, Warrendale, PA, p. 845.
[18] G. Sauthoff, *Diffusion in Ordered Alloys*, B. Fultz, R.W. Chan, D. Gupta, eds., TMS, Warrendale, PA, 1993, p. 205.
[19] H. Oikawa, *The Processing, Properties and Applications of Metallic and Ceramic Materials,* Warley, UK, 1992, p. 383.
[20] J. Kumpfert, *Adv. Eng. Mater.* 3 (2001) 851.
[21] R.S. Mishra, T.K. Nandy, P.K. Sagar, A.K. Gogia, and D. Banerjee. *Trans. India Inst. Met.* 49 (1996) 331.
[22] N.S. Stoloff, D.A. Alven, and C.G. McKamey. *Nickel and Iron Aluminides: Processing, Properties, and Applications,* ASM International, Materials Park, OH, 1997, p. 65.
[23] Y.W. Kim, *J. Metals* 46 (1994) 31.
[24] Y. W. Kim, *J. Metals* 41 (1989) 24.
[25] R.M. Moreno and M.T. Pérez-Prado. *In situ analysis of the high temperature deformation and fracture mechanisms of a γ-tial alloy*, Doctoral Thesis, 2014, p. 9-10.
[26] F. Appel, J. D. H. Paul, M. Oehring. *γ-Titanium Aluminide Alloys*. John Wiley & Sons (2011), p. 6.
[27] E.L. Hall and S.C. Huang, *Acta mater*. 38 (1990) 539.
[28] S.C. Huang and E.L. Hall. *Metall. Trans. A*, 22 (1991) 427.
[29] F. Appel, J. D. H. Paul, M. Oehring. *γ-Titanium Aluminide Alloys*. John Wiley & Sons, 2011, p. 58.

[30] J. Beddoes, W. Wallace, and L. Zhao. *Int. Mater. Reviews* 40 (1995) 197.
[31] W.J. Zhang and S.C. Deevi. *Structural Intermetallics 2001*, K.J. Hemker, D.M. Dimiduk, H. Clemens, R. Darolia, H. Inui, J.M. Larsen, V.K. Sikka, M. Thomas and J.D. Whittenberger, eds. TMS, Warrendale, PA, 2001, p.699.
[32] J. Beddoes, L. Zhao, P. Au, D. Dudzinsky, and J. Triantafillou, *Structural Intermetallics 1997*, M.V. Nathal, R. Darolia, C.T. Liu, P.L. Martin, D.B. Miracle, R. Wagner, and M. Yamaguchi, eds., TMS, Warrendale, PA, 1997, p. 109.
[33] M. Es-Souni, A. Bartels, and R. Wagner. *Mater. Sci. Eng. A*, 192/193 (1995) 698.
[34] D.B. Worth, J.W. Jones, and J.E. Allison. *Metall. Trans. A, 26 (1995) 2947.*
[35] Dynamic Systems Inc. *Gleeble Users Training 2010. Gleeble Systems and Applications.*
[36] B. Taylor and E. Weidmann. *Metallographic preparation of titanium.* Struers Application Notes.
[37] Oxford Instruments. *EBSD Explained. From data acquisition to advanced analysis.* 2015.
[38] S. Bystrzanowski et al. *Intermetallics.* 13, 2005, p. 515-524.
[39] QUE 99177 FIB lift out - YouTube.
[40] J. Mayer, L.A. Giannuzzi, T. Kamino and J. Michael. *TEM sample preparation and FIB-induced damage.* MRS Bulletin, Volume 32, May 2007.
[41] M.T. Pérez-Prado, G. González and O.A. Ruano. *Estudio de la deformación de aleaciones superplásticas de aluminio mediante análisis de texturas.* Doctoral Thesis, May 1998, p. 14.
[42] Wikipedia, the free encyclopedia. *Scanning electron microscope.*
[43] F. Appel, J. D. H. Paul, M. Oehring. *γ-Titanium Aluminide Alloys*. John Wiley & Sons, 2011, p. 125.